

Hemodynamic Deconvolution Demystified: Sparsity-Driven Regularization at Work

Eneko Uruñuela^{a,b,*}, Thomas A.W. Bolton^{c,d}, Dimitri Van De Ville^{c,e}, César Caballero-Gaudes^{a,*}

^a*Basque Center on Cognition, Brain and Language (BCBL), Donostia-San Sebastián, Spain.*

^b*University of the Basque Country (EHU/UPV), Donostia-San Sebastián, Spain.*

^c*Ecole Polytechnique Fédérale de Lausanne (EPFL), Lausanne, Switzerland.*

^d*Gamma Knife Center, Department of Clinical Neuroscience, Centre Hospitalier Universitaire Vaudois (CHUV), Lausanne, Switzerland*

^e*Faculty of Medicine, University of Geneva, Geneva, Switzerland*

Abstract

Deconvolution of the hemodynamic response is an important step to access short timescales of brain activity recorded by functional magnetic resonance imaging (fMRI). Albeit conventional deconvolution algorithms have been around for a long time (e.g., Wiener deconvolution), recent state-of-the-art methods based on sparsity-pursuing regularization are attracting increasing interest to investigate brain dynamics and connectivity with fMRI. This technical note revisits the main concepts underlying two main methods, Paradigm Free Mapping and Total Activation, in the most accessible way. Despite their apparent differences in the formulation, these methods are theoretically equivalent as they represent the synthesis and analysis sides of the same problem, respectively. We demonstrate this equivalence in practice with their best-available implementations using both simulations, with different signal-to-noise ratios, and experimental fMRI data acquired during a motor task and resting-state. We evaluate the parameter settings that lead to equivalent results, and showcase the potential of these algorithms compared to other common approaches. This note is useful for practitioners interested in gaining a better understanding of state-of-the-art hemodynamic deconvolution, and aims to answer questions that practitioners often have regarding the differences between the two methods.

Keywords: fMRI deconvolution, paradigm free mapping, total activation, temporal regularization

1. Introduction

Functional magnetic resonance imaging (fMRI) data analysis is often directed to identify and disentangle the neural processes that occur in different brain regions during task or at rest. As the blood oxygenation level-dependent (BOLD) signal of fMRI is only a proxy for neuronal activity mediated through neurovascular coupling, an intermediate step that estimates the activity-inducing signal, at the timescale of fMRI, from the BOLD timeseries can be useful. Conventional analysis of task fMRI data relies on the general linear models (GLM) to establish statistical parametric maps of brain activity by regression of the empirical timecourses against hypothetical ones built from

*Corresponding authors

Email addresses: e.urunuela@bcbl.eu (Eneko Uruñuela), c.caballero@bcbl.eu (César Caballero-Gaudes)

9 the knowledge of the experimental paradigm. However, timing information of the paradigm can be
10 unknown, inaccurate, or insufficient in some scenarios such as naturalistic stimuli, resting-state, or
11 clinically-relevant assessments.

12 Deconvolution and methods alike are aiming to estimate neuronal activity by undoing the blurring
13 effect of the hemodynamic response, characterized as a hemodynamic response function (HRF).
14 Given the inherently ill-posed nature of hemodynamic deconvolution, due to the strong temporal
15 low-pass characteristics of the HRF, the key is to introduce additional constraints in the estimation
16 problem that are typically expressed as regularizers. For instance, the so-called Wiener deconvolution
17 is expressing a “minimal energy” constraint on the deconvolved signal, and has been used
18 in the framework of psychophysiological interaction analysis to compute the interaction between a
19 seed’s activity-inducing timecourse and an experimental modulation (Glover, 1999; Gitelman et al.,
20 2003; Gerchen et al., 2014; Di and Biswal, 2018; Freitas et al., 2020). Complementarily, the interest
21 in deconvolution has increased to explore time-varying activity in resting-state fMRI data (Preti
22 et al., 2017; Keilholz et al., 2017; Lurie et al., 2020; Bolton et al., 2020). In that case, the aim is
23 to gain better insights of the neural signals that drive functional connectivity at short time scales,
24 as well as learning about the spatio-temporal structure of functional components that dynamically
25 construct resting-state networks and their interactions (Karahanoğlu and Ville, 2017).

26 Deconvolution of the resting-state fMRI signal has illustrated the significance of transient, sparse
27 spontaneous events (Petridou et al., 2012; Allan et al., 2015) that refine the hierarchical clusterization
28 of functional networks (Karahanoğlu et al., 2013) and reveal their temporal overlap based
29 on their signal innovations not only in the human brain (Karahanoğlu and Ville, 2015), but also
30 in the spinal cord (Kinany et al., 2020). Similar to task-related studies, deconvolution allows to
31 investigate modulatory interactions within and between resting-state functional networks (Di and
32 Biswal, 2013, 2015). In addition, decoding of the deconvolved spontaneous events allows to decipher
33 the flow of spontaneous thoughts and actions across different cognitive and sensory domains while
34 at rest (Karahanoğlu and Ville, 2015; Gonzalez-Castillo et al., 2019; Tan et al., 2017). Beyond findings
35 on healthy subjects, deconvolution techniques have also proven its utility in clinical conditions
36 to characterize functional alterations of patients with a progressive stage of multiple sclerosis at
37 rest (Bommarito et al., 2020), to find functional signatures of prodromal psychotic symptoms and
38 anxiety at rest on patients suffering from schizophrenia (Zöller et al., 2019), to detect the foci of
39 interictal events in epilepsy patients without an EEG recording (Lopes et al., 2012; Karahanoglu
40 et al., 2013), or to study functional dissociations observed during non-rapid eye movement sleep
41 that are associated with reduced consolidation of information and impaired consciousness (Tarun
42 et al., 2020).

43 The algorithms for hemodynamic deconvolution can be classified based on the assumed hemo-
44 dynamic model and the optimization problem used to estimate the neuronal-related signal. Most
45 approaches assume a linear time-invariant model for the hemodynamic response that is inverted
46 by means of variational (regularized) least squares estimators (Glover, 1999; Gitelman et al., 2003;
47 Gaudes et al., 2010, 2012, 2013; Caballero-Gaudes et al., 2019; Hernandez-Garcia and Ulfarsson,
48 2011; Karahanoglu et al., 2013; Cherkaooui et al., 2019; Costantini et al., 2021; Hütel et al., 2021),
49 logistic functions (Bush and Cisler, 2013; Bush et al., 2015; Loula et al., 2018), probabilistic mixture
50 models (Pidnebesna et al., 2019), convolutional autoencoders (Hütel et al., 2018) or nonparamet-
51 ric homomorphic filtering (Sreenivasan et al., 2015). Alternatively, several methods have also been
52 proposed to invert non-linear models of the neuronal and hemodynamic coupling (Riera et al., 2004;
53 Friston et al., 2008; Havlicek et al., 2011; Aslan et al., 2016; Madi and Karameh, 2017; Ruiz-Euler
54 et al., 2018).

55 Among the variety of approaches, those based on regularized least squares estimators have been
 56 employed more often due to their appropriate performance at small spatial scales (e.g., voxelwise).
 57 Relevant for this work, two different formulations can be established for the regularized least-
 58 squares deconvolution problem, either based on a synthesis- or analysis-based model (Elad et al.,
 59 2007; Ortelli and van de Geer, 2019). The rationale of the synthesis-based model is that we know
 60 or suspect that the true signal (here, the neuronally-driven BOLD component of the fMRI signal)
 61 can be represented as a linear combination of predefined patterns or dictionary atoms (for instance,
 62 the hemodynamic response function). In contrast, the analysis-based approach considers that the
 63 true signal is analyzed by some relevant operator and the resulting signal is small (i.e., sparse).

64 As members of the groups that developed Paradigm Free Mapping (synthesis-based) and Total
 65 Activation (analysis-based) deconvolution methods for fMRI data analysis, we are often contacted
 66 by researchers who want to know about the similarities and differences between the two methods
 67 and which one is better. It depends—and to clarify this point, this note revisits synthesis- and
 68 analysis-based deconvolution methods for fMRI data and comprises four sections. First, we present
 69 the theory behind these two deconvolution approaches based on regularized least squares estima-
 70 tors that promote sparsity: Paradigm Free Mapping (PFM) (Gaudes et al., 2013) — available in
 71 AFNI as *3dPFM*¹ and *3dMEPFM*² for single-echo and multi-echo data, respectively — and Total
 72 Activation (TA) (Karahanoglu et al., 2013) — available as part of the *iCAPs toolbox*³. We describe
 73 the similarities and differences in their analytical formulations, and how they can be related to
 74 each other. Next, we assess their performance controlling for a fair comparison on simulated and
 75 experimental data. Finally, we discuss their benefits and shortcomings and conclude with our vision
 76 on potential extensions and developments.

77 2. Theory

78 2.1. Notations and definitions

79 Matrices of size N rows and M columns are denoted by boldface capital letters, e.g., $\mathbf{X} \in \mathbb{R}^{N \times M}$,
 80 whereas column vectors of length N are denoted as boldface lowercase letters, e.g., $\mathbf{x} \in \mathbb{R}^N$. Scalars
 81 are denoted by lowercase letters, e.g., k . Continuous functions are denoted by brackets, e.g., $h(t)$,
 82 while discrete functions are denoted by square brackets, e.g., $x[k]$. The Euclidean norm of a matrix
 83 \mathbf{X} is denoted as $\|\mathbf{X}\|_2$, the ℓ_1 -norm is denoted by $\|\mathbf{X}\|_1$ and the Frobenius norm is denoted by
 84 $\|\mathbf{X}\|_F$. The discrete integration (**L**) and difference (**D**) operators are defined as:

$$\mathbf{L} = \begin{bmatrix} 1 & 0 & \dots & & \\ 1 & 1 & 0 & \dots & \\ 1 & 1 & 1 & 0 & \dots \\ \vdots & \ddots & \ddots & \ddots & \ddots \end{bmatrix}, \quad \mathbf{D} = \begin{bmatrix} 1 & 0 & \dots & & \\ 1 & -1 & 0 & \dots & \\ 0 & \ddots & \ddots & \ddots & \dots \\ \vdots & \ddots & 0 & 1 & -1 \end{bmatrix}.$$

85 2.2. Conventional general linear model analysis

Conventional general linear model (GLM) analysis puts forward a number of regressors incor-
 porating the knowledge about the paradigm or behavior. For instance, the timing of epochs for

¹https://afni.nimh.nih.gov/pub/dist/doc/program_help/3dPFM.html

²https://afni.nimh.nih.gov/pub/dist/doc/program_help/3dMEPFM.html

³<https://c4science.ch/source/iCAPs/>

a certain condition can be modeled as an indicator function $p(t)$ (e.g., Dirac functions for event-related designs or box-car functions for block-designs) convolved with the hemodynamic response function (HRF) $h(t)$, and sampled at TR resolution (Friston et al., 1994, 1998; Boynton et al., 1996; Cohen, 1997):

$$x(t) = p * h(t) \rightarrow x[k] = p * h(k \cdot \text{TR}).$$

The vector $\mathbf{x} = [x[k]]_{k=1,\dots,N} \in \mathbb{R}^N$ then constitutes the regressor modelling the hypothetical response, and several of them can be stacked as columns of the design matrix $\mathbf{X} = [\mathbf{x}_1 \dots \mathbf{x}_L] \in \mathbb{R}^{N \times L}$, leading to the well-known GLM formulation:

$$\mathbf{y} = \mathbf{X}\boldsymbol{\beta} + \mathbf{e}, \quad (1)$$

where the empirical timecourse $\mathbf{y} \in \mathbb{R}^N$ is explained by a linear combination of the regressors in \mathbf{X} weighted by the parameters in $\boldsymbol{\beta} \in \mathbb{R}^L$ and corrupted by additive noise $\mathbf{e} \in \mathbb{R}^N$. Under independent and identically distributed Gaussian assumptions of the latter, the maximum likelihood estimate of the parameter weights reverts to the ordinary least-squares estimator; i.e., minimizing the residual sum of squares between the fitted model and measurements. The number of regressors L is typically much less than the number of measurements N , and thus the regression problem is over-determined and does not require additional constraints or assumptions (Henson and Friston, 2007).

In the deconvolution approach, no prior knowledge of the hypothetical response is taken into account, and the purpose is to estimate the deconvolved activity-inducing signal \mathbf{s} from the measurements \mathbf{y} , which can be formulated as the signal model

$$\mathbf{y} = \mathbf{H}\mathbf{s} + \mathbf{e}, \quad (2)$$

where $\mathbf{H} \in \mathbb{R}^{N \times N}$ is a Toeplitz matrix that represents the discrete convolution with the HRF, and $\mathbf{s} \in \mathbb{R}^N$ is a length- N vector with the unknown activity-inducing signal. Note that the temporal resolution of the activity-inducing signal and the corresponding Toeplitz matrix is generally assumed to be equal to the TR of the acquisition, but it could also be higher if an upsampled estimate is desired. Despite the apparent similarity with the GLM equation, there are two important differences. First, the multiplication with the design matrix of the GLM is an expansion as a weighted linear combination of its columns, while the multiplication with the HRF matrix represents a convolution operator. Second, determining \mathbf{s} is an ill-posed problem given the nature of the HRF. As it can be seen intuitively, the convolution matrix \mathbf{H} is highly collinear (i.e., its columns are highly correlated) due to large overlap between shifted HRFs (see Figure 2C), thus introducing uncertainty in the estimates of \mathbf{s} when noise is present. Consequently, additional assumptions under the form of regularization terms (or priors) in the estimate are needed to reduce their variance. In the least squares sense, the optimization problem to solve is given by

$$\hat{\mathbf{s}} = \arg \min_{\mathbf{s}} \frac{1}{2} \|\mathbf{y} - \mathbf{H}\mathbf{s}\|_2^2 + \Omega(\mathbf{s}). \quad (3)$$

The first term quantifies data fitness, which can be justified as the log-likelihood term derived from Gaussian noise assumptions, while the second term $\Omega(\mathbf{s})$ brings in regularization and can be interpreted as a prior on the activity-inducing signal. For example, the ℓ_2 -norm of \mathbf{s} (i.e., $\Omega(\mathbf{s}) = \lambda \|\mathbf{s}\|_2^2$) is imposed for ridge regression or Wiener deconvolution, which introduces a trade-off between the data fit term and “energy” of the estimates that is controlled by the regularization parameter λ . regularized terms are related to the elastic net (i.e., $\Omega(\mathbf{x}) = \lambda_1 \|\mathbf{x}\|_2^2 + \lambda_2 \|\mathbf{x}\|_1$) [REF].

99 2.3. Paradigm Free Mapping

In paradigm free mapping (PFM), the formulation of Eq. (3) was considered equivalently as fitting the measurements using the atoms of the HRF dictionary (i.e., columns of \mathbf{H}) with corresponding weights (entries of \mathbf{s}). This model corresponds to a synthesis formulation. In Gaudes et al. 2013 a sparsity-pursuing regularization term was introduced on \mathbf{s} , which in a strict way reverts to choosing $\Omega(\mathbf{s}) = \lambda\|\mathbf{s}\|_0$ as the regularization term and solving the optimization problem (Bruckstein et al., 2009). However, finding the optimal solution to the problem demands an exhaustive search across all possible combinations of the columns of \mathbf{H} . Hence, a pragmatic solution is to solve the convex-relaxed optimization problem for the l_1 -norm, commonly known as Basis Pursuit Denoising (Chen et al., 2001) or equivalently as the least absolute shrinkage and selection operator (LASSO) (Tibshirani, 1996):

$$\hat{\mathbf{s}} = \arg \min_{\mathbf{s}} \frac{1}{2} \|\mathbf{y} - \mathbf{H}\mathbf{s}\|_2^2 + \lambda\|\mathbf{s}\|_1, \quad (4)$$

100 which provides fast convergence to a global solution. Imposing sparsity on the activity-inducing
 101 signal implies that it is assumed to be well represented by a reduced subset of few non-zero coeffi-
 102 cients at the fMRI timescale, which in turn trigger event-related BOLD responses. Hereinafter, we
 103 refer to this assumption as the *spike model*. However, even if PFM was developed as a spike model,
 104 its formulation in Eq.(4) can be extended to estimate the innovation signal, i.e., the derivative of
 105 the activity-inducing signal, as shown in section 2.5.

106 2.4. Total Activation

Alternatively, deconvolution can be formulated as if the signal to be recovered directly fits the measurements and at the same time satisfies some suitable regularization, which leads to

$$\hat{\mathbf{x}} = \arg \min_{\mathbf{x}} \frac{1}{2} \|\mathbf{y} - \mathbf{x}\|_2^2 + \Omega(\mathbf{x}). \quad (5)$$

107 Under this analysis formulation, total variation (TV), i.e., the l_1 -norm of the derivative $\Omega(\mathbf{x}) =$
 108 $\lambda\|\mathbf{Dx}\|_1$, is a powerful regularizer since it favors recovery of piecewise-constant signals (Chambolle,
 109 2004). Going beyond, the approach of generalized TV introduces an additional differential operator
 110 $\mathbf{D}_\mathbf{H}$ in the regularizer that can be tailored as the inverse operator of a linear system (Karahanoglu
 111 et al., 2011), that is, $\Omega(\mathbf{x}) = \lambda\|\mathbf{DD}_\mathbf{H}\mathbf{x}\|_1$. In the context of hemodynamic deconvolution, To-
 112 tal Activation is proposed for which the discrete operator $\mathbf{D}_\mathbf{H}$ is derived from the inverse of the
 113 continuous-domain linearized Balloon-Windkessel model (Buxton et al., 1998; Friston et al., 2000).
 114 The interested reader is referred to (Khalidov et al., 2011; Karahanoglu et al., 2011; Karahanoglu
 115 et al., 2013) for a detailed description of this derivation.

Therefore, the solution of the Total Activation (TA) problem

$$\hat{\mathbf{x}} = \arg \min_{\mathbf{x}} \frac{1}{2} \|\mathbf{y} - \mathbf{x}\|_2^2 + \lambda\|\mathbf{DD}_\mathbf{H}\mathbf{x}\|_1 \quad (6)$$

116 will yield the activity-related signal \mathbf{x} for which the activity-inducing signal $\mathbf{s} = \mathbf{D}_\mathbf{H}\mathbf{x}$ and the
 117 so-called innovation signal $\mathbf{u} = \mathbf{Ds}$, i.e., the derive of the activity-inducing signal, will also be
 118 available, as they are required for the regularization. We refer to modeling the activity-inducing
 119 signal based on the innovation signal as the *block model*. Nevertheless, even if TA was originally
 120 developed as a block model, its formulation in Eq.(6) can be made equivalent to the spike model
 121 as shown in section 2.5.

122 *2.5. Unifying both perspectives*

123 PFM and TA are based on the synthesis- and analysis-based formulation of the deconvolution
124 problem, respectively. They are also tailored for the spike and block model, respectively. In the first
125 case, the recovered deconvolved signal is synthesized to be matched to the measurements, while in
126 the second case, the recovered signal is directly matched to the measurements but needs to satisfy
127 its analysis in terms of deconvolution. This also corresponds to using the forward or backward
128 model of the hemodynamic system, respectively. Hence, it is possible to make both approaches
129 equivalent (Elad et al., 2007)⁴.

130 To start with, TA can be made equivalent to PFM by adapting it for the spike model; i.e., when
131 removing the derivative operator \mathbf{D} of the regularizer in Eq. (6), it can be readily verified that
132 replacing in that case $\mathbf{x} = \mathbf{H}\mathbf{s}$ leads to identical equations and thus both assume a spike model,
133 since \mathbf{H} and $\mathbf{D}_\mathbf{H}$ will cancel out each other (Karahanoğlu et al., 2011)⁵.

Conversely, the PFM spike model can also accommodate the TA block model by modifying Eq. (4) with the forward model $\mathbf{y} = \mathbf{H}\mathbf{L}\mathbf{u} + \mathbf{e}$. Here, the activity-inducing signal \mathbf{s} is rewritten in terms of the innovation signal \mathbf{u} as $\mathbf{s} = \mathbf{L}\mathbf{u}$ where the matrix \mathbf{L} is the first-order integration operator (Cherkaoui et al., 2019; Uruñuela et al., 2020). This way, PFM can estimate the innovation signal \mathbf{u} as follows:

$$\hat{\mathbf{u}} = \arg \min_{\mathbf{u}} \frac{1}{2} \|\mathbf{y} - \mathbf{H}\mathbf{L}\mathbf{u}\|_2^2 + \lambda \|\mathbf{u}\|_1, \quad (7)$$

134 and becomes equivalent to TA by replacing $\mathbf{u} = \mathbf{DD}_\mathbf{H}\mathbf{x}$, and thus adopting the block model. Based
135 on the previous equations (4), (6) and (7), it is clear that both PFM and TA can operate under the
136 spike and block models, providing a convenient signal model according to the different assumptions
137 of the underlying neuronal-related signal. This work evaluates the core of the two techniques; i.e.,
138 the regularized least-squares problem with temporal regularization without considering the spatial
139 regularization term originally incorporated in TA. For the remainder of this paper, we will use the
140 PFM and TA formalisms with both spike and block models.

141 *2.6. Algorithms and parameter selection*

142 Despite their apparent resemblance, the practical implementations of the PFM and TA methods
143 proposed different algorithms to solve the corresponding optimization problem and select an
144 adequate regularization parameter λ (Gaudes et al., 2013; Karahanoğlu et al., 2013). The PFM
145 implementation available in AFNI employs the least angle regression (LARS) (Efron et al., 2004),
146 whereas the TA implementation uses the fast iterative shrinkage-thresholding algorithm (FISTA)
147 (Beck and Teboulle, 2009). The blue box in Figure 1 provides a descriptive view of the iterative
148 *modus operandi* of the two algorithms.

149 On the one hand, LARS is a homotopy approach that computes all the possible solutions to
150 the optimization problem and their corresponding value of λ ; i.e., the regularization path, and
151 the solution according to the Bayesian Information Criterion (BIC) (Schwarz, 1978), was recom-
152 mended as the most appropriate in the case of PFM approaches since AIC often tends to overfit
153 the signal (Gaudes et al., 2013; Caballero-Gaudes et al., 2019).

On the other hand, FISTA is an extension of the classical gradient algorithm that provides fast
convergence for large-scale problems. In the case of FISTA though, the regularization parameter λ

⁴Without dwelling into technicalities, for total variation, this equivalence is correct up to the constant, which is in the null space of the derivative operator.

⁵Again, this holds up to elements of the null space.

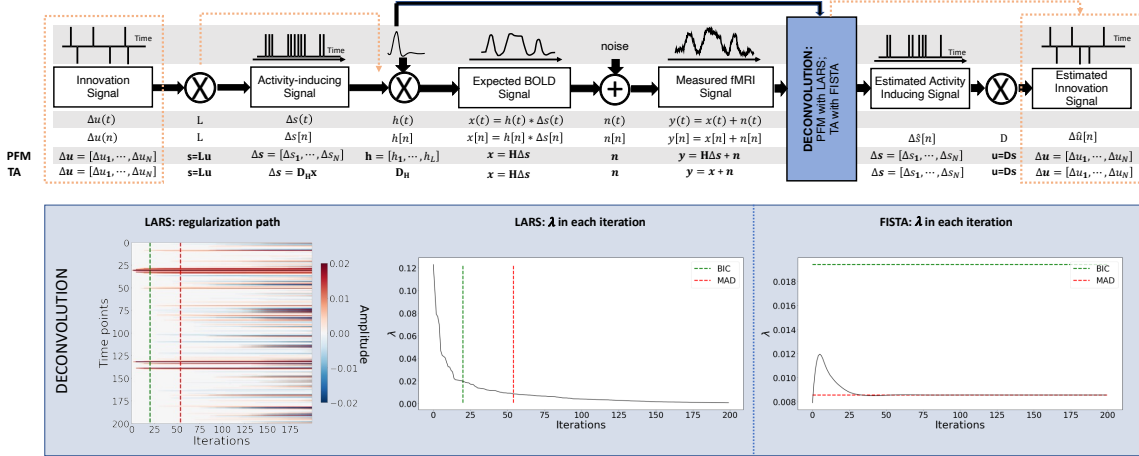


Figure 1: Flowchart detailing the different steps of the fMRI signal and the deconvolution methods described. The orange arrows indicate the flow to estimate the innovation signals, i.e., the derivative of the activity-inducing signal. The blue box depicts the iterative *modus operandi* of the two algorithms used in this paper to solve the paradigm free mapping (PFM) and total activation (TA) deconvolution problems. The plot on the left shows the regularization path obtained with the least angle regression (LARS) algorithm, where the x-axis illustrates the different iterations of the algorithm, the y-axis represents points in time, and the color describes the amplitude of the estimated signal. The middle plot depicts the decreasing values of λ for each iteration of LARS as the regularization path is computed. The green and red dashed lines in both plots illustrate the Bayesian information criterion (BIC) and median absolute deviation (MAD) solutions, respectively. Comparatively, the changes in λ when the fast iterative shrinkage-thresholding algorithm (FISTA) method is made to converge to the MAD estimate of the noise are shown on the right. Likewise, the λ corresponding to the BIC and MAD solutions are shown with dashed lines.

must be selected prior to solving the problem, but can be updated in every iteration so that the residuals of the data fit converge to an estimated noise level of the data $\hat{\sigma}$:

$$\lambda^{n+1} = \frac{N\hat{\sigma}}{\frac{1}{2}\|\mathbf{y} - \mathbf{x}^n\|_F^2} \lambda^n, \quad (8)$$

where x^n is the n^{th} iteration estimate, λ^n and λ^{n+1} are the n^{th} and $n+1^{th}$ iteration values for the regularization parameter λ , and N is the number of points in the time-course. The pre-estimated noise level can be obtained as the median absolute deviation (MAD) of the fine-scale wavelet coefficients (Daubechies, order 3) of the fMRI timecourse. The MAD criterion has been adopted in TA (Karahanoglu et al., 2013). Of note, similar formulations based on the MAD estimate have also been applied in PFM formulations (Gaudes et al., 2012, 2011).

3. Methods

3.1. Simulated data

In order to compare the two methods while controlling for their correct performance, we created a simulation scenario that can be found in the GitHub repository shared in Section 6. For the sake of illustration, we describe here the simulations corresponding to a timecourse with a duration of 400 seconds (TR = 2 s) where the activity-inducing signal includes 5 events, which are convolved with

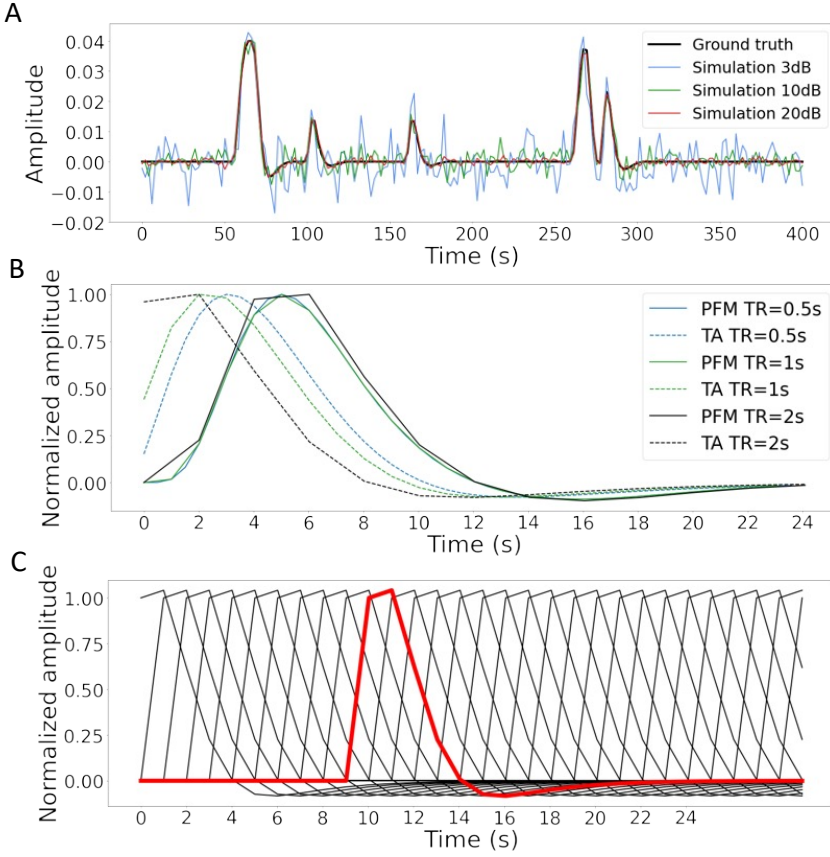


Figure 2: A) Simulated signal with different SNRs (20 dB, 10 dB and 3 dB) and ground truth given in signal percentage change (SPC). B) Canonical HRF models typically used by PFM (solid line) and TA (dashed line) at TR = 0.5 s (blue), TR = 1 s (green) and TR = 2 s (black). Without loss of generality, the waveforms are scaled to unit amplitude for visualization. C) Representation of shifted HRFs at TR = 2 s that build the design matrix for PFM when the HRF model has been matched to that in TA. The red line corresponds to one of the columns of the HRF matrix.

the canonical HRF. Different noise sources (physiological, thermal, and motion-related) were also added and we simulated three different scenarios with varying signal-to-noise ratios (SNR = [20 dB, 10 dB, 3 dB]) that represent high, medium and low contrast-to-noise ratios as shown in Figure 2A. Noise was created following the procedure in (Gaudes et al., 2013) as the sum of uncorrelated Gaussian noise and sinusoidal signals to simulate a realistic noise model with thermal noise, cardiac and respiratory physiological fluctuations, respectively. The physiological signals were generated as

$$\sum_{i=1}^2 \frac{1}{2^{i-1}} (\sin(2\pi f_{r,i}t + \phi_{r,i}) + \sin(2\pi f_{c,i}t + \phi_{c,i})), \quad (9)$$

162 with up to second-order harmonics per cardiac ($f_{c,i}$) and respiratory ($f_{r,i}$) component that were
163 randomly generated following normal distributions with variance 0.04 and mean if_r and if_c , for
164 $i = [1, 2]$. We set the fundamental frequencies to $f_r = 0.3$ Hz for the respiratory component (Birn
165 et al., 2006)) and $f_c = 1.1$ Hz for the cardiac component (Shmueli et al., 2007)). The phases of
166 each harmonic ϕ were randomly selected from a uniform distribution between 0 and 2π radians.
167 To simulate physiological noise that is proportional to the change in BOLD signal, a variable ratio
168 between the physiological (σ_P) and the thermal (σ_0) noise was modeled as $\sigma_P/\sigma_0 = a(tSNR)^b + c$,
169 where $a = 5.01 \times 10^{-6}$, $b = 2.81$, and $c = 0.397$, following the experimental measures available in
170 Table 3 from (Triantafyllou et al., 2005)).

171 *3.2. Experimental data*

172 To compare the performance of the two approaches as well as illustrate their operation, we
173 employ two representative experimental datasets.

174 **Motor task dataset:** One healthy subject was scanned in a 3T MR scanner (Siemens) under a
175 Basque Center on Cognition, Brain and Language Review Board-approved protocol. T2*-weighted
176 multi-echo fMRI data was acquired with a simultaneous-multislice multi-echo gradient echo-planar
177 imaging sequence, kindly provided by the Center of Magnetic Resonance Research (University
178 of Minnesota, USA) (Feinberg et al., 2010; Moeller et al., 2010; Setsompop et al., 2011), with the
179 following parameters: 340 temporal frames, 52 slices, Partial-Fourier = 6/8, voxel size = $2.4 \times 2.4 \times 3$
180 mm 3 , TR = 1.5 s, TEs = 10.6/28.69/46.78/64.87/82.96 ms, flip angle = 70°, multiband factor =
181 4, GRAPPA = 2.

182 During the fMRI acquisition, the subject performed a motor task consisting of five different
183 movements (left-hand finger tapping, right-hand finger tapping, moving the left toes, moving the
184 right toes and moving the tongue) that were visually cued through a mirror located on the head
185 coil. These conditions were randomly intermixed every 16 seconds, and were only repeated once
186 the entire set of stimuli were presented. Data preprocessing consisted of first, discarding the first 10
187 volumes of the functional data to achieve a steady state of magnetization. Then, image realignment
188 to the skull-stripped single-band reference image (SBRef) was computed on the first echo, and the
189 estimated rigid-body spatial transformation was applied to all other echoes (Jenkinson et al., 2012;
190 Jenkinson and Smith, 2001). A brain mask obtained from the SBRef volume was applied to all the
191 echoes and the different echo timeseries were optimally combined (OC) voxelwise by weighting each
192 timeseries contribution by its T2* value (Posse et al., 1999). AFNI (Cox, 1996) was employed for a
193 detrending of up to 4th-order Legendre polynomials, within-brain spatial smoothing (3 mm FWHM)
194 and voxelwise signal normalization to percentage change. Finally, distortion field correction was
195 performed on the OC volume with Topup (Andersson et al., 2003), using the pair of spin-echo EPI
196 images with reversed phase encoding acquired before the ME-EPI acquisition (Glasser et al., 2016).

197 **Resting-state datasets:** One healthy subject was scanned in a 3T MR scanner (Siemens)
198 under a Basque Center on Cognition, Brain and Language Review Board-approved protocol. Two
199 runs of T2*-weighted fMRI data were acquired during resting-state, each with 10 min duration,
200 with 1) a standard gradient-echo echo-planar imaging sequence (monoband) (TR = 2000 ms, TE
201 = 29 ms, flip-angle = 78°, matrix size = 64 × 64, voxel size = 3 × 3 × 3 mm 3 , 33 axial slices
202 with interleaved acquisition, slice gap = 0.6 mm) and 2) a simultaneous-multislice gradient-echo
203 echo-planar imaging sequence (multiband factor = 3, TR = 800 ms, TE = 29 ms, flip-angle = 60°,
204 matrix size = 64 × 64, voxel size = 3 × 3 × 3 mm 3 , 42 axial slices with interleaved acquisition, no
205 slice gap). Single-band reference images were also collected in both resting-state acquisitions for
206 head motion realignment. Field maps were also obtained to correct for field distortions.

207 During both acquisitions, participants were instructed to keep their eyes open, fixating a white
208 cross that they saw through a mirror located on the head coil, and not to think about anything
209 specific. The data was pre-processed using AFNI (Cox, 1996). First, volumes corresponding to the
210 initial 10 seconds were removed to allow for a steady-state magnetization. Then, the voxel time-
211 series were despiked to reduce large-amplitude deviations and slice-time corrected. Inhomogeneities
212 caused by magnetic susceptibility were corrected with FUGUE (FSL) using the field map images
213 (Jenkinson et al., 2012). Next, functional images were realigned to a base volume (monoband: volume
214 with the lowest head motion; multiband: single-band reference image). Finally, a simultaneous
215 nuisance regression step was performed comprising up to 6th-order Legendre polynomials, low-pass
216 filtering with a cutoff frequency of 0.25 Hz (only on multiband data to match the frequency content
217 of the monoband), 6 realignment parameters plus temporal derivatives, 5 principal components
218 of white matter (WM), 5 principal components of lateral ventricle voxels (anatomical CompCor)
219 (Behzadi et al., 2007) and 5 principal components of the brain’s edge voxels ,(Patriat et al., 2015).
220 WM, CSF and brain’s edge-voxel masks were obtained from Freesurfer tissue and brain segmentations.
221 In addition, scans with potential artifacts were identified and censored when the euclidean
222 norm of the temporal derivative of the realignment parameters (ENORM) was larger than 0.4, and
223 the proportion of voxels adjusted in the despiking step exceeded 10%.

224 *3.3. Selection of the hemodynamic response function*

225 In their original formulations, PFM and TA specify the discrete-time HRF in different ways.
226 For PFM, the continuous-domain specification of the canonical double-gamma HRF (Henson and
227 Friston, 2007) is sampled at the TR and then put as shifted impulse responses to build the matrix
228 **H**. In the case of TA, however, the continuous-domain linearized version of the balloon-windkessel
229 model is discretized to build the linear differential operator in **D_H**. While the TR only changes
230 the resolution of the HRF shape for PFM, the impact of an equivalent impulse response of the
231 discretized differential operator at different TR is more pronounced. As shown in Figure 2B, longer
232 TR leads to equivalent impulse responses of TA that are shifted in time, provoking a lack of the
233 initial baseline and rise of the response. We refer the reader to Figure S1 to see the differences
234 in the estimation of the activity-inducing and innovation signals when both methods use the HRF
235 in their original formulation. To avoid differences between PFM and TA based on their built-in
236 HRF, we choose to build the synthesis operator **H** with shifted versions of the HRF given by the
237 TA analysis operator (e.g., see Figure 2C for the TR=2s case).

238 *3.4. Selection of the regularization parameter*

239 We use the simulated data to compare the performance of the two deconvolution algorithms
240 with both BIC and MAD criteria to set the regularization parameter λ (see section 2.6). We also
241 evaluate if the algorithms behave differently in terms of the estimation of the activity-inducing
242 signal \hat{s} using the spike model described in (4) and the block model based on the innovation signal
243 \hat{u} in (7).

244 For selection based on the BIC, LARS was initially performed with the PFM deconvolution
245 model to obtain the solution for every possible λ in the regularization path. Then, the values of λ
246 corresponding to the BIC optimum were adopted to solve the TA deconvolution model by means
247 of FISTA.

248 For a selection based on the MAD estimate of the noise, we apply the temporal regularization in
249 its original form for TA, whereas for PFM the selected λ corresponds to the solution whose residuals
250 have the closest standard deviation to the estimated noise level of the data $\hat{\sigma}$.

251 3.5. Analyses in experimental fMRI data

Difference between approaches: To assess the discrepancies between both approaches when applied on experimental fMRI data, we calculate the square root of the sum of squares of the differences (RSSD) between the activity-inducing signals estimated with PFM and TA on the three experimental datasets as

$$\text{RSSD} = \sqrt{\frac{1}{N} \sum_{k=1}^N (\hat{s}_{\text{PFM}}[k] - \hat{s}_{\text{TA}}[k])^2}, \quad (10)$$

252 where N is the number of timepoints of the acquisition. The RSSD of the innovation signals $\hat{\mathbf{u}}$ was
253 computed equally.

254 **Task fMRI data:** In the analysis of the motor task data, we evaluate the performance of PFM
255 and TA in comparison with a conventional General Linear Model analysis (*3dDeconvolve* in AFNI)
256 that takes advantage of the information about the duration and onsets of the motor trials. Given
257 the block design of the motor task, we only make this comparison with the block model.

258 **Resting-state fMRI data:** We also illustrate the usefulness of deconvolution approaches
259 in the analysis of resting-state data where information about the timings of neuronal-related
260 BOLD activity cannot be predicted. Apart from being able to explore individual maps of de-
261 convolved activity (i.e., innovation signals, activity-inducing signals, or hemodynamic signals) at
262 the temporal resolution of the acquisition (or deconvolution), here we calculate the [average extreme](#)
263 [points of the activity-inducing and innovation maps \(considering enough points were not available](#)
264 [to perform a clustering step\)](#) and illustrate how popular approaches like co-activation patterns
265 (CAPs) (Tagliazucchi et al., 2012; Liu et al., 2018) and innovation-driven co-activation patterns
266 (iCAPs) (Karahanoğlu and Ville, 2015) can be applied on the deconvolved signals to reveal pat-
267 terns of coordinated brain activity. To achieve this, we calculate the average time-series in a seed
268 of 9 voxels located in the precuneus, supramarginal gyrus, and occipital gyri independently, and
269 solve the deconvolution problem to find the activity-inducing and innovation signals in the seeds.
270 We then apply a 95th percentile threshold and average the maps of the time-frames that survive the
271 threshold. Finally, we apply the same procedure to the original— i.e., non-deconvolved— signal in
272 the seed and compare the results with the widely-used seed correlation approach.

273 4. Results

274 4.1. Performance based on the regularization parameter

275 Figure 3A shows the regularization paths of PFM and TA side by side obtained for the spike
276 model of Eq. (4) for SNR=3 dB. The solutions for all three SNR conditions are shown in Figures S2
277 and S3. Starting from the maximum λ corresponding to a null estimate and for decreasing values
278 of λ , LARS computes a new estimate at the value of λ that reduces the sparsity promoted by the
279 l_1 -norm and causes a change in the active set of non-zero coefficients of the estimate (i.e., a zero
280 coefficient becomes non-zero or vice versa) as shown in the horizontal axis of the heatmaps. Vertical
281 dashed lines depict the selection of the regularization parameter based on the BIC, and thus, the
282 colored coefficients indicated by these depict the estimated activity-inducing signal $\hat{\mathbf{s}}$. Figure 3B
283 illustrates the resulting estimates of the activity-inducing and activity-related hemodynamic signals
284 when basing the selection of λ on the BIC for SNR=3 dB. Given that the regularization paths of
285 both approaches are identical, it can be clearly observed that the BIC-based estimates are identical
286 too for the corresponding λ . Thus, Figures 3A, 3B, S2 and S3 demonstrate that, regardless of

the simulated SNR condition, the spike model of both deconvolution algorithms produces identical regularization paths when the same HRF and regularization parameters are applied, and hence, identical estimates of the activity-inducing signal \hat{s} and neuronal-related hemodynamic signal \hat{x} . Likewise, Figure 3C demonstrates that the regularization paths for the block model defined in Eqs. (6) and (7) also yield virtually identical estimates of the innovation signals for both PFM and TA methods. Again, the BIC-based selection of λ is identical for both PFM and TA. As illustrated in Figure 3D, the estimates of the innovation signal u also show no distinguishable differences between the algorithms. Figures 3 A-D demonstrate that both PFM and TA yield equivalent regularization paths and estimates of the innovation signal and activity-inducing signal regardless of the simulated SNR condition when applying the same HRF and regularization parameters with the block and spike models.

As for selecting λ with the MAD criterion defined in Eq. (8), Figure 3E depicts the estimated activity-inducing and activity-related signals for the simulated low-SNR setting using the spike model, while Figure 3F shows the estimated signals corresponding to the block model. Both plots in Figure 3E and F depict nearly identical results between PFM and TA with both models. Given that the regularization paths of both techniques are identical, minor dissimilarities are owing to the slight differences in the selection of λ due to the quantization of the values returned by LARS.

4.2. Performance on experimental data

Figure 4 depicts the RSSD maps revealing differences between PFM and TA estimates for the spike (Figure 4A and C) and block (Figure 4B and D) models when applied to the three experimental fMRI datasets. The RSSD values are virtually negligible (i.e., depicted in yellow) in most of the within-brain voxels and lower than the amplitude of the estimates of the activity-inducing and innovation signals. Based on the maximum value of the range shown in each image, we observe that the similarity between both approaches is more evident for the spike model (with both selection criteria) and the block model with the BIC selection. However, given the different approaches used for the selection of the regularization parameter λ based on the MAD estimate of the noise, higher RSSD values can be observed with the largest differences occurring in gray matter voxels. These areas also correspond to low values of λ (see Figure S4) and MAD estimates of the noise (see Figure S5), while the highest values are visible in regions with signal dropouts, ventricles, and white matter.

Figure 5 depicts the results of the analysis of the Motor dataset with the PFM and TA algorithms using the BIC selection of λ (see Figure S6 for results with MAD selection), as well as a conventional GLM approach. The Activation Time Series (top left), calculated as the sum of squares of all voxel amplitudes (positive vs. negative) for a given moment in time, obtained with PFM and TA show nearly identical patterns. These ATS help to summarize the four dimensional information available in the results across the spatial domain and identify instances of significant BOLD activity. The second to sixth rows show the voxel timeseries and the corresponding activity-related, activity-inducing and innovation signals obtained with PFM using the BIC criterion of representative voxels in the regions activated in each of the motor tasks. The TA-estimated time-series are not shown because they were virtually identical. The maps shown on the right correspond to statistical parametric maps obtained with the GLM for each motor condition ($p < 0.001$) as well as the maps of the PFM and TA estimates at the onsets of individual motor events (indicated with arrows in the timecourses). The estimated activity-related, activity-inducing and innovation signals clearly reveal the activity patterns of each condition in the task, as they exhibit a BOLD response locked to the onset and duration of the conditions. Overall, activity maps of the innovation signal obtained

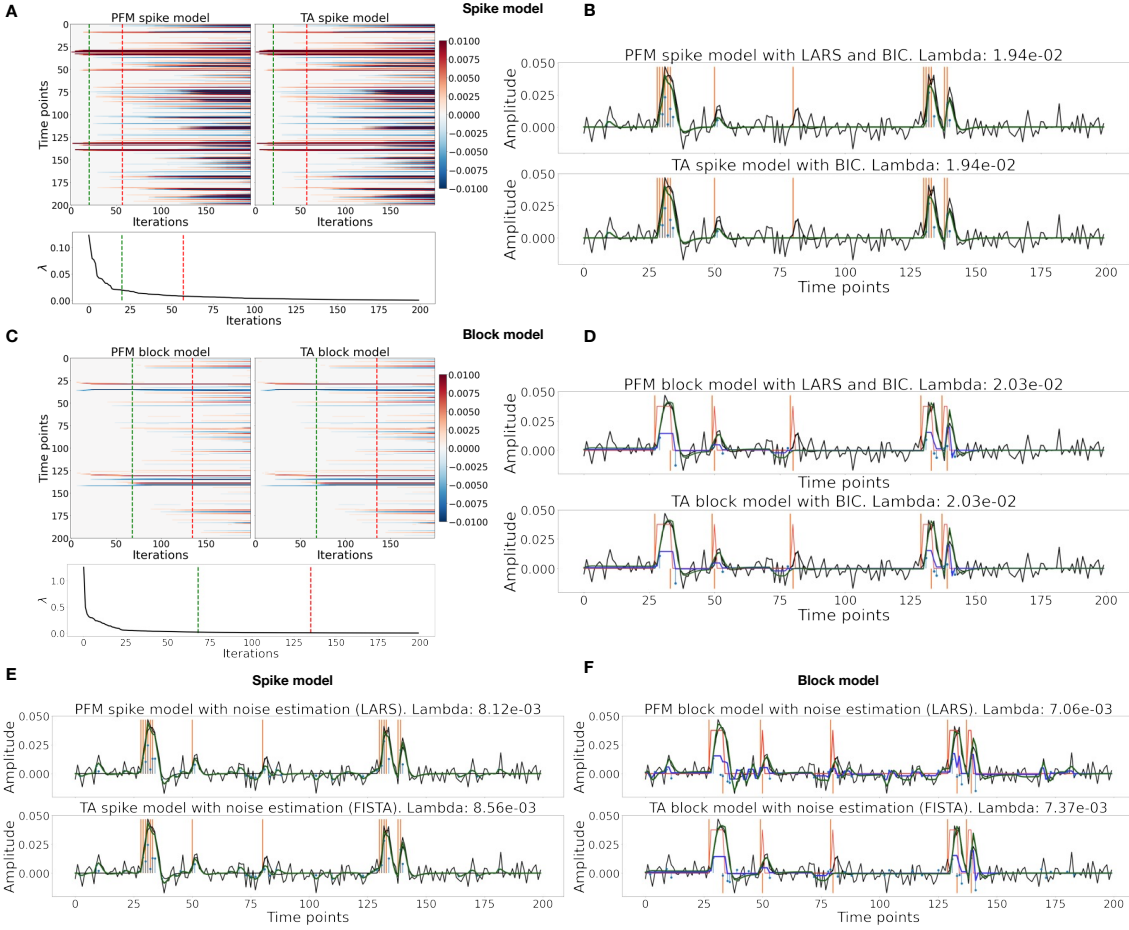


Figure 3: (A) Heatmap of the regularization paths of the activity-inducing signals (spike model) estimated with PFM and TA as a function of λ for the simulated data with SNR = 3 dB (x-axis: increasing number of iterations or λ as given by LARS; y-axis: time; color: amplitude). Vertical lines denote iterations corresponding to the BIC (dashed line) and MAD (dotted line) selection of λ . (B) Estimated activity-inducing (blue) and activity-related (green) signals with a selection of λ based on the BIC. Orange and red lines depict the ground truth. (C) Heatmap of the regularization paths of the innovation signals (block model) estimated with PFM and TA as a function of λ for the simulated data with SNR = 3 dB. (D) Estimated innovation (blue), activity-inducing (darker blue), and activity-related (green) signals with a selection of λ based on the BIC. (E) Activity-inducing and activity-related (fit, \times) signals estimated with PFM (top) and TA (bottom) when λ is selected based on the MAD method with the spike model, and (F) with the block model for the simulated data with SNR = 3 dB.

with PFM and TA highly resemble those obtained with a GLM for individual events, with small differences arising from the distinct specificity of the GLM and deconvolution analyses. Notice that the differences observed with the different approaches to select λ based on the MAD estimate shown in Figure 4 are reflected on the ATS shown in Figure S6 as well.

As an illustration of the insights that deconvolution methods can provide in the analysis of

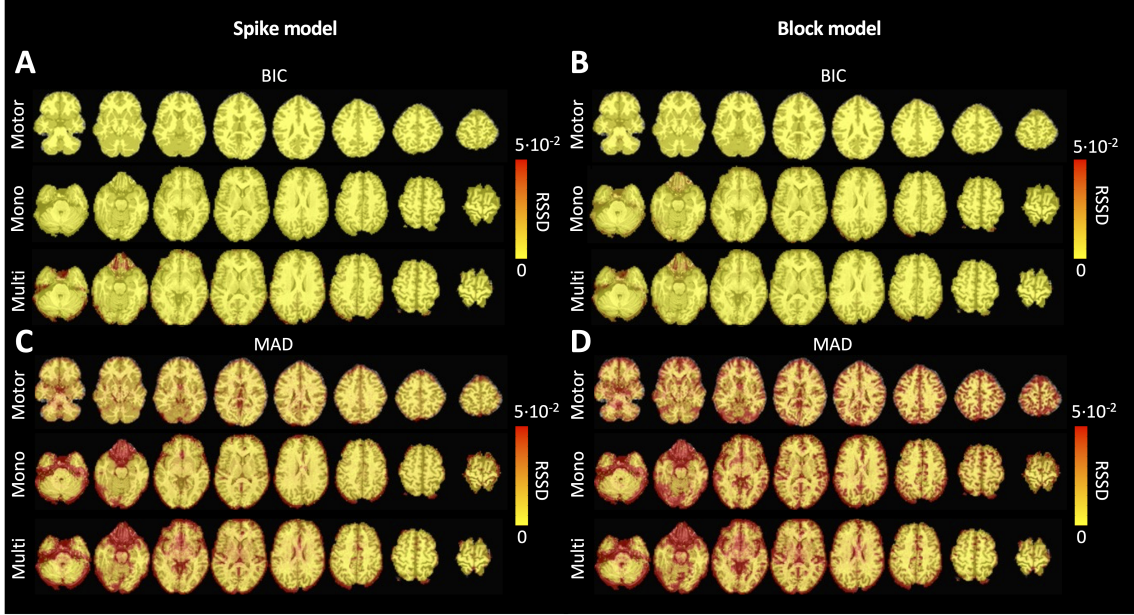


Figure 4: Square root of the sum of squared differences (RSSD) between the estimates obtained with PFM and TA for (A) spike model (activity-inducing signal) and BIC selection of λ , (B) block model (innovation signal) and BIC selection, (C) spike model (activity-inducing signal) and MAD selection, (D) block model (innovation signal) and MAD selection. RSSD maps are shown for the three experimental fMRI datasets: the motor task (Motor), the monoband resting-state (Mono), and the multiband resting-state (Multi) datasets.

resting-state data, Figure 6 depicts the [average activity-inducing and innovation maps of common resting-state networks](#) obtained from thresholding and averaging the activity-inducing and innovation signals, respectively, estimated from the resting-state multiband data using PFM with a selection of λ based on the BIC. The [average activity-inducing maps](#) obtained via deconvolution show spatial patterns of the default mode network (DMN), dorsal attention network (DAN), and visual network (VIS) that highly resemble the maps obtained with conventional seed correlation analysis using Pearson's correlation, and the [average maps of extreme points](#) of the signal (i.e., with no deconvolution). With deconvolution, the [average activity-inducing maps seem to depict more accurate spatial delineation](#) (i.e., less smoothness) than those obtained from the original data, while maintaining the structure of the networks. The BIC-informed selection of λ yields spatial patterns of [average activity-inducing and innovation maps](#) that are more sparse than those obtained with a selection of λ based on the MAD estimate (see Figure S7). Furthermore, the spatial patterns of the [average innovation maps](#) based on the innovation signals using the block model yield complementary information to those obtained with the activity-inducing signal since iCAPs allow to reveal regions with synchronous innovations, i.e., with the same upregulating and downregulating events. For instance, it is interesting to observe that the structure of the visual network nearly disappears in its corresponding [average innovation maps](#), suggesting the existence of different temporal neuronal patterns across voxels in the primary and secondary visual cortices.

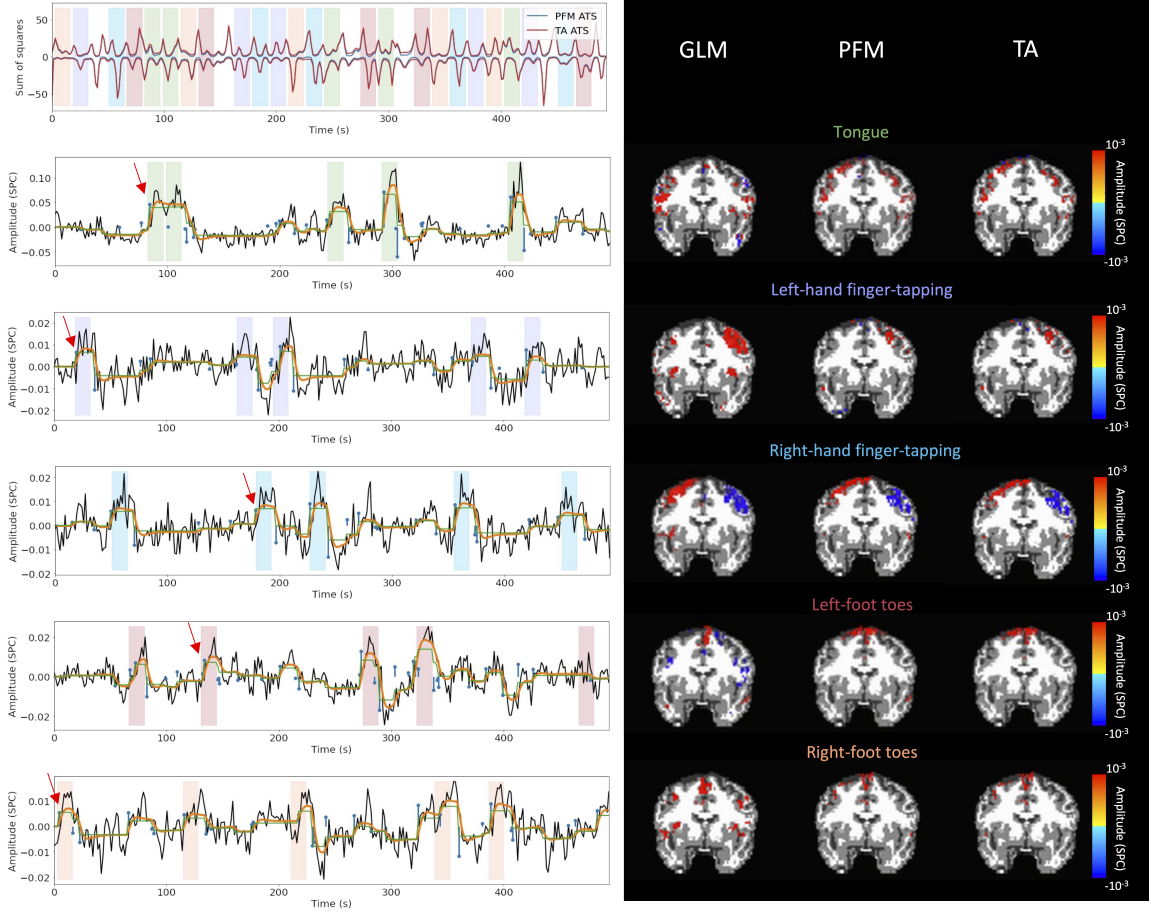


Figure 5: Activity maps of the motor task using a selection of λ based on the BIC estimate. Row 1: Activation time-series (ATS) of the innovation signals estimated by PFM (in blue) or TA (in red) calculated as the sum of squares of all voxels at every timepoint. Positive-valued and negative-valued contributions were separated into two distinct time-courses. Color-bands indicate the onset and duration of each condition in the task (green: tongue motion, purple: left-hand finger-tapping, blue: right-hand finger-tapping, red: left-foot toes motion, orange: right-foot toes motion). Rows 2-6: time-series of a representative voxel for each task with the PFM-estimated innovation (blue), PFM-estimated activity-inducing (green), and activity-related (i.e., fitted, orange) signals, with their corresponding GLM, PFM, and TA maps on the right (representative voxels indicated with green arrows). Amplitudes are given in signal percentage change (SPC). The maps shown on the right are sampled at the time-points labeled with the red arrows and display the innovation signals at these moments across the whole brain.

355 5. Discussion

356 Hemodynamic deconvolution can be formulated using a synthesis- and analysis-based approach
 357 as proposed by PFM and TA, respectively. This work demonstrates that the theoretical equivalence
 358 of **both approaches** is confirmed in practice given virtually identical results when the same HRF
 359 model and equivalent regularization parameters are employed. Hence, we argue that previously
 360 observed differences in performance can be explained by specific settings, such as the HRF model

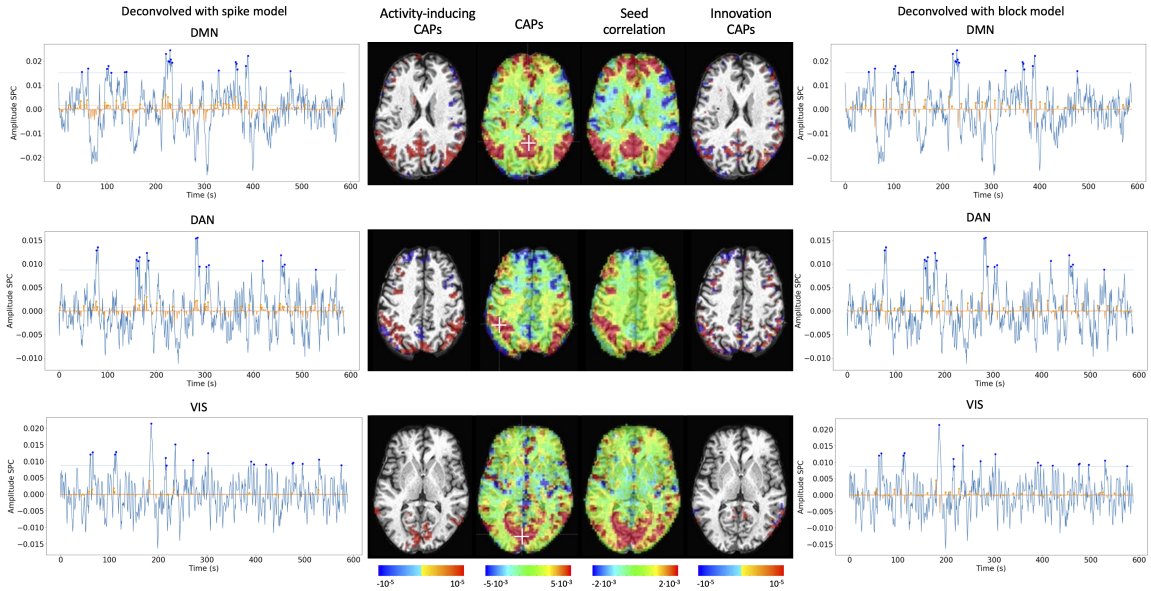


Figure 6: Average activity-inducing (left) and innovation (right) maps obtained from PFM-estimated activity-inducing and innovation signals, respectively, using a BIC-based selection of λ . Time-points selected with a 95th percentile threshold (horizontal lines) are shown over the average time-series (blue) in the seed region (white cross) and the deconvolved signals, i.e., activity inducing (left) and innovation (right) signals (orange). Average maps of extreme points and seed correlation maps are illustrated in the center.

and selection of the regularization parameter, convergence thresholds, as well as the addition of a spatial regularization term in the spatiotemporal TA formulation (Karahanoglu et al., 2013). For instance, the use of PFM with the spike model in (Tan et al., 2017) was seen not to be ideal due to the prolonged trials in the paradigm, which better fit the block model as described here (7). Similarly, all the works using the iCAPs approach, and thus the TA implementation for deconvolution (Kinany et al., 2020; Zöller et al., 2019; Pirondini et al., 2022), could alternatively use the PFM approach with the block model and adding a spatial regularization term, which would yield identical results providing the same criterion is used to select the regularization parameters. However, given the equivalence of the temporal deconvolution, incorporating extra spatial or temporal regularization terms in the optimization problem should not modify this equivalence providing convex operators are employed. For a convex optimization problem, with a unique global solution, iterative shrinkage thresholding procedures alternating between the different regularization terms guarantee convergence; e.g., the generalized forward-backward splitting (Raguet et al., 2013) algorithm originally employed for TA. Our findings are also in line with the equivalence of analysis and synthesis methods in under-determined cases ($N \leq V$) demonstrated in (Elad et al., 2007) and (Ortelli and van de Geer, 2019). Using a lower regularization parameter (i.e., penalty on the amplitude of the estimates) makes the estimates more similar to the least-squares solution, which results in higher sensitivity in detecting events. Conversely, employing a higher λ leads to higher specificity at the cost of a decrease in sensitivity. Still, we have shown that a slight difference in the selection of the regularization parameter can lead to small differences in the estimated signals when employing the

381 block model with the MAD selection of λ . However, since their regularization paths are equivalent,
382 the algorithms can easily be forced to converge to the same selection of λ , thus resulting in identical
383 estimated signals.

384 Nevertheless, the different formulations of analysis and synthesis deconvolution models bring
385 along different kinds of flexibility. One notable advantage of PFM is that it can readily incorporate
386 any HRF as part of the synthesis operator (Elad et al., 2007), only requiring the sampled HRF at the
387 desired temporal resolution, which is typically equal to the TR of the acquisition. Conversely, TA
388 relies upon the specification of the discrete differential operator that inverts the HRF, which needs
389 to be derived either by the inverse solution of the sampled HRF impulse response, or by discretizing
390 a continuous-domain differential operator motivated by a biophysical model. The more versatile
391 structure of PFM allows for instance an elegant extension of the algorithm to multi-echo fMRI
392 data (Caballero-Gaudes et al., 2019) where multiple measurements relate to a common underlying
393 signal. Therefore, the one-to-many synthesis scenario (i.e., from activity-inducing to several activity-
394 related signals) is more cumbersome to express using TA; i.e., a set of differential operators should
395 be defined and the differences between their outputs constrained. Conversely, the one-to-many
396 analysis scenario (i.e., from the measurements to several regularizing signals) is more convenient
397 to be expressed by TA; e.g., combining spike and block regularizers. While the specification of the
398 differential operator in TA only indirectly controls the HRF, the use of the derivative operator to
399 enforce the block model, instead of the integrator in PFM, impacts positively the stability and rate
400 of the convergence of the optimization algorithms. Moreover, analysis formulations can be more
401 suitable for online applications that are still to be explored in fMRI data, but are employed for
402 calcium imaging deconvolution (Friedrich et al., 2017; Jewell et al., 2019), and which have been
403 applied for offline calcium deconvolution (Farouj et al., 2020).

404 Deconvolution techniques can be used before more downstream analysis of brain activity in terms
405 of functional network organization as they estimate interactions between voxels or brain regions that
406 occur at the activity-inducing level, and are thus less affected by the slowness of the hemodynamic
407 response compared to when the BOLD signals are analyzed directly. In addition, deconvolution
408 approaches hold a close parallelism to recent methodologies aiming to understand the dynamics of
409 neuronal activations and interactions at short temporal resolution and that focus on extreme events
410 of the fMRI signal (Lindquist et al., 2007). As an illustration, Figure 6 shows that the innovation-
411 or activity-inducing CAPs computed from deconvolved events in a single resting-state fMRI dataset
412 closely resemble the conventional CAPs computed directly from extreme events of the fMRI signal
413 (Liu and Duyn, 2013; Liu et al., 2013, 2018; Cifre et al., 2020a,b; Zhang et al., 2020; Tagliazucchi
414 et al., 2011, 2012, 2016; Rolls et al., 2021). Similarly, we hypothesize that these extreme events
415 will also show a close resemblance to intrinsic ignition events (Deco and Kringsbach, 2017; Deco
416 et al., 2017). As shown in the maps, deconvolution approaches can offer a more straightforward
417 interpretability of the activation events and resulting functional connectivity patterns. Here, CAPs
418 were computed as the average of spatial maps corresponding to the events of a single dataset.
419 Beyond simple averaging, clustering algorithms (e.g., K-means and consensus clustering) can be
420 employed to discern multiple CAPs or iCAPs at the whole-brain level for a large number of subjects.
421 Previous findings based on iCAPs have for instance revealed organizational principles of brain
422 function during rest (Karahanoglu and Ville, 2015) and sleep (Tarun et al., 2021) in healthy controls,
423 next to alterations in 22q11ds (Zoeller et al., 2019) and multiple sclerosis (Bommarito et al., in
424 press). Next to CAPs-inspired approaches, dynamic functional connectivity has recently been
425 investigated with the use of co-fluctuations and edge-centric techniques (Faskowitz et al., 2020;
426 Esfahlani et al., 2020; Jo et al., 2021; Sporns et al., 2021; van Oort et al., 2018). The activation

427 time series shown in Figure 5 aim to provide equivalent information to the root of sum of squares
428 timecourses used in edge-centric approaches, where timecourses with peaks delineate instances
429 of significant brain activity. Future work could address which type of information is redundant
430 or distinct across these frameworks. In summary, these examples illustrate that deconvolution
431 techniques can be employed prior to other computational approaches and could serve as an effective
432 way of denoising the fMRI data. We foresee an increase in the number of studies that take advantage
433 of the potential benefits of using deconvolution methods prior to functional connectivity analyses.

434 In sum, hemodynamic deconvolution approaches using sparsity-driven regularization are valuable
435 tools to complete the fMRI processing pipeline. Although the two approaches examined in
436 detail here provide alternative representations of the BOLD signals in terms of innovation and
437 activity-inducing signals, their current implementations have certain limitations, calling for further
438 developments or more elaborate models, where some of them have been initially addressed in the
439 literature. One relevant focus is to account for the variability in HRF that can be observed in
440 different regions of the brain. First, variability in the temporal characteristics of the HRF can arise
441 from differences in stimulus intensity and patterns, as well as with short inter-event intervals like in
442 fast cognitive processes or experimental designs (Yeşilyurt et al., 2008; Chen et al., 2021; Sadaghiani
443 et al., 2009; Polimeni and Lewis, 2021). Similarly, the HRF shape at rest might differ from the
444 canonical HRF commonly used for task-based fMRI data analysis. A wide variety of HRF patterns
445 could be elicited across the whole brain and possibly detected with sufficiently large signal-to-noise
446 ratio, e.g., (Gonzalez-Castillo et al., 2012) showed two gamma-shaped responses at the onset and
447 the end of the evoked trial, respectively. This unique HRF shape would be deconvolved as two
448 separate events with the conventional deconvolution techniques. The impact of HRF variability
449 could be reduced using structured regularization terms along with multiple basis functions (Gaudes
450 et al., 2012) or procedures that estimate the HRF shape in an adaptive fashion in both analysis
451 (Farouj et al., 2019) and synthesis formulations (Cherkaoui et al., 2020a).

452 Another avenue of research consists in leveraging spatial information by adopting multivariate
453 deconvolution approaches that operate at the whole-brain level, instead of working voxelwise and
454 beyond regional regularization terms (e.g. as proposed in Karahanoglu et al. 2013). Operating
455 at the whole-brain level would open the way for methods that consider shared neuronal activity
456 using mixed norm regularization terms (Uruñuela-Tremiño et al., 2019) or can capture long-range
457 neuronal cofluctuations using low rank decompositions (Cherkaoui et al., 2020a). For example,
458 multivariate deconvolution approaches could yield better localized activity patterns while reducing
459 the effect of global fluctuations such as respiratory artifacts, which cannot be modelled at the voxel
460 level Uruñuela et al. 2021.

461 Similar to solving other inverse problems by means of regularized estimators, the selection of
462 the regularization parameter is critical to correctly estimate the neuronal-related signal. Hence,
463 methods that take advantage of a more robust selection of the regularization parameter could
464 considerably yield more reliable estimates of the neuronal-related signal. For instance, the stability
465 selection (Meinshausen and Bühlmann, 2010; Uruñuela et al., 2020) procedure could be included
466 to the deconvolution problem to ensure that the estimated coefficients are obtained with high
467 probability. Furthermore, an important issue of regularized estimation is that the estimates are
468 biased with respect to the true value. In that sense, the use of non-convex $\ell_{p,q}$ -norm regularization
469 terms (e.g., $p < 1$) can reduce this bias while maintaining the sparsity constraint, at the cost of
470 potentially converging to a local minima of the regularized estimation problem. In practice, these
471 approaches could avoid the optional debiasing step that overcomes the shrinkage of the estimates and
472 obtain a more accurate and less biased fit of the fMRI signal (Gaudes et al., 2013; Caballero-Gaudes

et al., 2019). Finally, cutting-edge developments on physics-informed deep learning techniques for inverse problems (Akçakaya et al., 2021; Monga et al., 2021; Ongie et al., 2020; Cherkaoui et al., 2020b) could be transferred for deconvolution by considering the biophysical model of the hemodynamic system and could potentially offer algorithms with reduced computational time and more flexibility.

6. Code and data availability

The code and materials used in this work can be found in the following GitHub repository: https://github.com/eurunuela/pfm_vs_ta. We encourage the reader to explore the parameters (e.g., SNR, varying HRF options and mismatch between algorithms, TR, number of events, onsets, and durations) in the provided Jupyter notebooks. Likewise, the data used to produce the figures can be found in <https://osf.io/f3ryg/>.

7. Acknowledgements

We thank Stefano Moia and Vicente Ferrer for data availability, and Younes Farouj for valuable comments on the manuscript. This research was funded by the Spanish Ministry of Economy and Competitiveness (RYC-2017-21845), the Basque Government (BERC 2018-2021, PIB_2019_104, PRE_2020_2_0227), and the Spanish Ministry of Science, Innovation and Universities (PID2019-105520GB-100), and the Swiss National Science Foundation (grant 205321_163376).

8. CRediT

Eneko Uruñuela: Conceptualisation, Methodology, Software, Formal Analysis, Investigation, Data Curation, Writing (OD), Writing (RE), Visualisation, Funding acquisition. Thomas A.W. Bolton: Conceptualisation, Methodology, Writing (RE). Dimitri Van de Ville: Conceptualisation, Methodology, Writing (RE). César Caballero-Gaudes: Conceptualisation, Methodology, Software, Formal Analysis, Investigation, Data Curation, Writing (OD), Writing (RE), Visualisation, Funding acquisition.

References

- Akçakaya, M., Yaman, B., Chung, H., Ye, J.C., 2021. Unsupervised deep learning methods for biological image reconstruction [arXiv:2105.08040](https://arxiv.org/abs/2105.08040).
- Allan, T.W., Francis, S.T., Caballero-Gaudes, C., Morris, P.G., Liddle, E.B., Liddle, P.F., Brookes, M.J., Gowland, P.A., 2015. Functional connectivity in MRI is driven by spontaneous BOLD events. PLOS ONE 10, e0124577. doi:10.1371/journal.pone.0124577.
- Andersson, J.L., Skare, S., Ashburner, J., 2003. How to correct susceptibility distortions in spin-echo echo-planar images: application to diffusion tensor imaging. NeuroImage 20, 870–888. doi:10.1016/s1053-8119(03)00336-7.
- Aslan, S., Cemgil, A.T., Akın, A., 2016. Joint state and parameter estimation of the hemodynamic model by particle smoother expectation maximization method. Journal of Neural Engineering 13, 046010. doi:10.1088/1741-2560/13/4/046010.

- 509 Beck, A., Teboulle, M., 2009. A fast iterative shrinkage-thresholding algorithm for linear inverse
510 problems. *SIAM Journal on Imaging Sciences* 2, 183–202. doi:10.1137/080716542.
- 511 Behzadi, Y., Restom, K., Liau, J., Liu, T.T., 2007. A component based noise correction method
512 (CompCor) for BOLD and perfusion based fMRI. *NeuroImage* 37, 90–101. doi:10.1016/j.
513 *neuroimage*.2007.04.042.
- 514 Birn, R.M., Diamond, J.B., Smith, M.A., Bandettini, P.A., 2006. Separating respiratory-variation-
515 related fluctuations from neuronal-activity-related fluctuations in fMRI. *NeuroImage* 31, 1536–
516 1548. doi:10.1016/j.neuroimage.2006.02.048.
- 517 Bolton, T.A., Morgenroth, E., Preti, M.G., Ville, D.V.D., 2020. Tapping into multi-faceted human
518 behavior and psychopathology using fMRI brain dynamics. *Trends in Neurosciences* 43, 667–680.
519 doi:10.1016/j.tins.2020.06.005.
- 520 Bommarito, G., Tarun, A., Farouj, Y., Preti, M.G., Petracca, M., Droby, A., Mendili, M.M.E.,
521 Inglese, M., Ville, D.V.D., 2020. Altered anterior default mode network dynamics in progressive
522 multiple sclerosis. *medRxiv* doi:10.1101/2020.11.26.20238923.
- 523 Bommarito, G., Tarun, A., Farouj, Y., Preti, M.G., Petracca, M., Droby, A., Mounir El Mendili,
524 M., Inglese, M., Van De Ville, D., in press. Altered anterior default mode network dynamics in
525 progressive multiple sclerosis. *Multiple Sclerosis Journal* doi:10.1177/13524585211018116.
- 526 Boynton, G.M., Engel, S.A., Glover, G.H., Heeger, D.J., 1996. Linear systems analysis of functional
527 magnetic resonance imaging in human v1. *The Journal of Neuroscience* 16, 4207–4221. doi:10.
528 1523/jneurosci.16-13-04207.1996.
- 529 Bruckstein, A.M., Donoho, D.L., Elad, M., 2009. From sparse solutions of systems of equations to
530 sparse modeling of signals and images. *SIAM Review* 51, 34–81. doi:10.1137/060657704.
- 531 Bush, K., Cisler, J., 2013. Decoding neural events from fMRI BOLD signal: A comparison of
532 existing approaches and development of a new algorithm. *Magnetic Resonance Imaging* 31, 976–
533 989. doi:10.1016/j.mri.2013.03.015.
- 534 Bush, K., Zhou, S., Cisler, J., Bian, J., Hazaroglu, O., Gillispie, K., Yoshigoe, K., Kilts, C.,
535 2015. A deconvolution-based approach to identifying large-scale effective connectivity. *Magnetic
536 Resonance Imaging* 33, 1290–1298. doi:10.1016/j.mri.2015.07.015.
- 537 Buxton, R.B., Wong, E.C., Frank, L.R., 1998. Dynamics of blood flow and oxygenation changes
538 during brain activation: the balloon model. *Magnetic resonance in medicine* 39, 855–864.
- 539 Caballero-Gaudes, C., Moia, S., Panwar, P., Bandettini, P.A., Gonzalez-Castillo, J., 2019. A
540 deconvolution algorithm for multi-echo functional MRI: Multi-echo sparse paradigm free mapping.
541 *NeuroImage* 202, 116081. doi:10.1016/j.neuroimage.2019.116081.
- 542 Chambolle, A., 2004. An algorithm for total variation minimization and applications. *Journal of
543 Mathematical imaging and vision* 20, 89–97.
- 544 Chen, J.E., Glover, G.H., Fultz, N.E., Rosen, B.R., Polimeni, J.R., Lewis, L.D., 2021. Investigating
545 mechanisms of fast BOLD responses: The effects of stimulus intensity and of spatial heterogeneity
546 of hemodynamics. *NeuroImage* 245, 118658. doi:10.1016/j.neuroimage.2021.118658.

- 547 Chen, S.S., Donoho, D.L., Saunders, M.A., 2001. Atomic decomposition by basis pursuit. SIAM
 548 review 43, 129–159.
- 549 Cherkaoui, H., Moreau, T., Halimi, A., Ciuciu, P., 2019. Sparsity-based blind deconvolution of
 550 neural activation signal in fMRI, in: ICASSP 2019 - 2019 IEEE International Conference on
 551 Acoustics, Speech and Signal Processing (ICASSP), IEEE. pp. 1323–1327. doi:10.1109/icassp.
 552 2019.8683358.
- 553 Cherkaoui, H., Moreau, T., Halimi, A., Leroy, C., Ciuciu, P., 2020a. Multivariate semi-blind
 554 deconvolution of fMRI time series. URL: <https://hal.archives-ouvertes.fr/hal-03005584>.
 555 working paper or preprint.
- 556 Cherkaoui, H., Sulam, J., Moreau, T., 2020b. Learning to solve TV regularised problems with
 557 unrolled algorithms 33, 11513–11524. URL: <https://proceedings.neurips.cc/paper/2020/file/84fec9a8e45846340fdf5c7c9f7ed66c-Paper.pdf>.
- 559 Cifre, I., Flores, M.T.M., Ochab, J.K., Chialvo, D.R., 2020a. Revisiting non-linear functional brain
 560 co-activations: directed, dynamic and delayed. arXiv:2007.15728.
- 561 Cifre, I., Zarepour, M., Horovitz, S.G., Cannas, S.A., Chialvo, D.R., 2020b. Further results on why
 562 a point process is effective for estimating correlation between brain regions. Papers in Physics
 563 12, 120003. doi:10.4279/pip.120003.
- 564 Cohen, M.S., 1997. Parametric analysis of fMRI data using linear systems methods. NeuroImage
 565 6, 93–103. doi:10.1006/nimg.1997.0278.
- 566 Costantini, I., Deriche, R., Deslauriers-Gauthier, S., 2021. A paradigm free regularization approach
 567 to recover brain activation from functional MRI data. bioRxiv doi:10.1101/2021.04.14.438942.
- 568 Cox, R.W., 1996. AFNI: Software for analysis and visualization of functional magnetic resonance
 569 neuroimages. Computers and Biomedical Research 29, 162–173. doi:10.1006/cbm.1996.0014.
- 570 Deco, G., Kringelbach, M.L., 2017. Hierarchy of information processing in the brain: A novel
 571 ‘intrinsic ignition’ framework. Neuron 94, 961–968. doi:10.1016/j.neuron.2017.03.028.
- 572 Deco, G., Tagliazucchi, E., Laufs, H., Sanjuán, A., Kringelbach, M.L., 2017. Novel intrinsic ignition
 573 method measuring local-global integration characterizes wakefulness and deep sleep. eNeuro 4.
 574 doi:10.1523/ENEURO.0106-17.2017.
- 575 Di, X., Biswal, B.B., 2013. Modulatory interactions of resting-state brain functional connectivity.
 576 PLoS ONE 8, e71163. doi:10.1371/journal.pone.0071163.
- 577 Di, X., Biswal, B.B., 2015. Characterizations of resting-state modulatory interactions in the human
 578 brain. Journal of Neurophysiology 114, 2785–2796. doi:10.1152/jn.00893.2014.
- 579 Di, X., Biswal, B.B., 2018. Toward task connectomics: Examining whole-brain task modulated
 580 connectivity in different task domains. Cerebral Cortex 29, 1572–1583. doi:10.1093/cercor/
 581 bhy055.
- 582 Efron, B., Hastie, T., Johnstone, I., Tibshirani, R., 2004. Least angle regression. The Annals of
 583 Statistics 32, 407–499. doi:10.1214/009053604000000067.

- 584 Elad, M., Milanfar, P., Rubinstein, R., 2007. Analysis versus synthesis in signal priors. *Inverse
585 Problems* 23, 947–968. doi:10.1088/0266-5611/23/3/007.
- 586 Esfahlani, F.Z., Jo, Y., Faskowitz, J., Byrge, L., Kennedy, D.P., Sporns, O., Betzel, R.F., 2020.
587 High-amplitude cofluctuations in cortical activity drive functional connectivity. *Proceedings of
588 the National Academy of Sciences* 117, 28393–28401. doi:10.1073/pnas.2005531117.
- 589 Farouj, Y., Karahanoglu, F.I., Ville, D.V.D., 2019. Bold signal deconvolution under uncertain
590 hÆmodynamics: A semi-blind approach, in: 2019 IEEE 16th International Symposium on
591 Biomedical Imaging (ISBI 2019), IEEE. IEEE. pp. 1792–1796. doi:10.1109/isbi.2019.8759248.
- 592 Farouj, Y., Karahanoglu, F.I., Ville, D.V.D., 2020. Deconvolution of sustained neural activity from
593 large-scale calcium imaging data 39, 1094–1103. doi:10.1109/tmi.2019.2942765.
- 594 Faskowitz, J., Esfahlani, F.Z., Jo, Y., Sporns, O., Betzel, R.F., 2020. Edge-centric functional
595 network representations of human cerebral cortex reveal overlapping system-level architecture.
596 *Nature neuroscience* 23, 1644–1654. doi:10.1038/s41593-020-00719-y.
- 597 Feinberg, D.A., Moeller, S., Smith, S.M., Auerbach, E., Ramanna, S., Glasser, M.F., Miller, K.L.,
598 Ugurbil, K., Yacoub, E., 2010. Multiplexed echo planar imaging for sub-second whole brain
599 FMRI and fast diffusion imaging. *PLoS ONE* 5, e15710. doi:10.1371/journal.pone.0015710.
- 600 Freitas, L.G., Bolton, T.A., Krikler, B.E., Jochaut, D., Giraud, A.L., Hüppi, P.S., Ville, D.V.D.,
601 2020. Time-resolved effective connectivity in task fMRI: Psychophysiological interactions of co-
602 activation patterns. *NeuroImage* 212, 116635. doi:10.1016/j.neuroimage.2020.116635.
- 603 Friedrich, J., Zhou, P., Paninski, L., 2017. Fast online deconvolution of calcium imaging data.
604 *PLOS Computational Biology* 13, e1005423. doi:10.1371/journal.pcbi.1005423.
- 605 Friston, K., Fletcher, P., Josephs, O., Holmes, A., Rugg, M., Turner, R., 1998. Event-related fMRI:
606 Characterizing differential responses. *NeuroImage* 7, 30–40. doi:10.1006/nimg.1997.0306.
- 607 Friston, K., Trujillo-Barreto, N., Daunizeau, J., 2008. DEM: A variational treatment of dynamic
608 systems. *NeuroImage* 41, 849–885. doi:10.1016/j.neuroimage.2008.02.054.
- 609 Friston, K.J., Jezzard, P., Turner, R., 1994. Analysis of functional MRI time-series. *Human Brain
610 Mapping* 1, 153–171. doi:10.1002/hbm.460010207.
- 611 Friston, K.J., Mechelli, A., Turner, R., Price, C.J., 2000. Nonlinear responses in fmri: the balloon
612 model, volterra kernels, and other hemodynamics. *NeuroImage* 12, 466–477.
- 613 Gaudes, C.C., Karahanoglu, F.I., Lazeyras, F., Ville, D.V.D., 2012. Structured sparse deconvolution
614 for paradigm free mapping of functional MRI data, in: 2012 9th IEEE International Symposium
615 on Biomedical Imaging (ISBI), IEEE. IEEE. pp. 322–325. doi:10.1109/isbi.2012.6235549.
- 616 Gaudes, C.C., Petridou, N., Dryden, I.L., Bai, L., Francis, S.T., Gowland, P.A., 2010. Detection
617 and characterization of single-trial fMRI bold responses: Paradigm free mapping. *Human Brain
618 Mapping* 32, 1400–1418. doi:10.1002/hbm.21116.

- 619 Gaudes, C.C., Petridou, N., Francis, S.T., Dryden, I.L., Gowland, P.A., 2013. Paradigm free
620 mapping with sparse regression automatically detects single-trial functional magnetic resonance
621 imaging blood oxygenation level dependent responses. *Human Brain Mapping* , n/a–n/adoi:10.
622 1002/hbm.21452.
- 623 Gaudes, C.C., Van De Ville, D., Petridou, N., Lazeyras, F., Gowland, P., 2011. Paradigm-free
624 mapping with morphological component analysis: Getting most out of fmri data, in: *Wavelets*
625 and Sparsity XIV, International Society for Optics and Photonics. p. 81381K.
- 626 Gerchen, M.F., Bernal-Casas, D., Kirsch, P., 2014. Analyzing task-dependent brain network changes
627 by whole-brain psychophysiological interactions: A comparison to conventional analysis. *Human*
628 *Brain Mapping* 35, 5071–5082. doi:10.1002/hbm.22532.
- 629 Gitelman, D.R., Penny, W.D., Ashburner, J., Friston, K.J., 2003. Modeling regional and psy-
630 chophysiologic interactions in fMRI: the importance of hemodynamic deconvolution. *NeuroImage*
631 19, 200–207. doi:10.1016/s1053-8119(03)00058-2.
- 632 Glasser, M.F., Smith, S.M., Marcus, D.S., Andersson, J.L.R., Auerbach, E.J., Behrens, T.E.J.,
633 Coalson, T.S., Harms, M.P., Jenkinson, M., Moeller, S., Robinson, E.C., Sotiroopoulos, S.N., Xu,
634 J., Yacoub, E., Ugurbil, K., Essen, D.C.V., 2016. The human connectome project's neuroimaging
635 approach. *Nature Neuroscience* 19, 1175–1187. doi:10.1038/nn.4361.
- 636 Glover, G.H., 1999. Deconvolution of impulse response in event-related BOLD fMRI1. *NeuroImage*
637 9, 416–429. doi:10.1006/nimg.1998.0419.
- 638 Gonzalez-Castillo, J., Caballero-Gaudes, C., Topolski, N., Handwerker, D.A., Pereira, F., Ban-
639 dettini, P.A., 2019. Imaging the spontaneous flow of thought: Distinct periods of cogni-
640 tion contribute to dynamic functional connectivity during rest. *NeuroImage* 202, 116129.
641 doi:10.1016/j.neuroimage.2019.116129.
- 642 Gonzalez-Castillo, J., Saad, Z.S., Handwerker, D.A., Inati, S.J., Brenowitz, N., Bandettini, P.A.,
643 2012. Whole-brain, time-locked activation with simple tasks revealed using massive averaging
644 and model-free analysis. *Proceedings of the National Academy of Sciences of the United States*
645 of America
- 109, 5487–5492. doi:10.1073/pnas.1121049109.
- 646 Havlicek, M., Friston, K.J., Jan, J., Brazdil, M., Calhoun, V.D., 2011. Dynamic modeling of
647 neuronal responses in fMRI using cubature kalman filtering. *NeuroImage* 56, 2109–2128. doi:10.
648 1016/j.neuroimage.2011.03.005.
- 649 Henson, R., Friston, K., 2007. Chapter 14 - convolution models for fmri, in: Friston, K., Ash-
650 burner, J., Kiebel, S., Nichols, T., Penny, W. (Eds.), *Statistical Parametric Mapping*. Academic
651 Press, London, pp. 178–192. URL: <https://www.sciencedirect.com/science/article/pii/B9780123725608500140>, doi:<https://doi.org/10.1016/B978-012372560-8/50014-0>.
- 653 Hernandez-Garcia, L., Ulfarsson, M.O., 2011. Neuronal event detection in fMRI time series using
654 iterative deconvolution techniques. *Magnetic Resonance Imaging* 29, 353–364. doi:10.1016/j.j.
655 mri.2010.10.012.
- 656 Hütel, M., Antonelli, M., Melbourne, A., Ourselin, S., 2021. Hemodynamic matrix factorization for
657 functional magnetic resonance imaging. *NeuroImage* 231, 117814. doi:10.1016/j.neuroimage.
658 2021.117814.

- 659 Hütel, M., Melbourne, A., Ourselin, S., 2018. Neural activation estimation in brain networks
660 during task and rest using BOLD-fMRI, in: Medical Image Computing and Computer Assisted
661 Intervention – MICCAI 2018, Springer. Springer International Publishing. pp. 215–222. doi:10.
662 1007/978-3-030-00931-1_25.
- 663 Jenkinson, M., Beckmann, C.F., Behrens, T.E., Woolrich, M.W., Smith, S.M., 2012. FSL. Neu-
664 roImage 62, 782–790. doi:10.1016/j.neuroimage.2011.09.015.
- 665 Jenkinson, M., Smith, S., 2001. A global optimisation method for robust affine registration of brain
666 images. Medical Image Analysis 5, 143–156. doi:10.1016/s1361-8415(01)00036-6.
- 667 Jewell, S.W., Hocking, T.D., Fearnhead, P., Witten, D.M., 2019. Fast nonconvex deconvolution of
668 calcium imaging data. Biostatistics 21, 709–726. doi:10.1093/biostatistics/kxy083.
- 669 Jo, Y., Faskowitz, J., Esfahlani, F.Z., Sporns, O., Betzel, R.F., 2021. Subject identification us-
670 ing edge-centric functional connectivity. NeuroImage 238, 118204. doi:10.1016/j.neuroimage.
671 2021.118204.
- 672 Karahanoglu, F.I., Bayram, İ., Ville, D.V.D., 2011. A signal processing approach to generalized
673 1-d total variation. IEEE Transactions on Signal Processing 59, 5265–5274. doi:10.1109/tsp.
674 2011.2164399.
- 675 Karahanoglu, F.I., Caballero-Gaudes, C., Lazeyras, F., Ville, D.V.D., 2013. Total activation: fMRI
676 deconvolution through spatio-temporal regularization. NeuroImage 73, 121–134. doi:10.1016/
677 j.neuroimage.2013.01.067.
- 678 Karahanoglu, F.I., Grouiller, F., Gaudes, C.C., Seeck, M., Vulliemoz, S., Ville, D.V.D., 2013.
679 Spatial mapping of interictal epileptic discharges in fMRI with total activation, in: 2013 IEEE
680 10th International Symposium on Biomedical Imaging, Ieee. IEEE. pp. 1500–1503. doi:10.1109/
681 isbi.2013.6556819.
- 682 Karahanoglu, F.I., Ville, D.V.D., 2015. Transient brain activity disentangles fMRI resting-state
683 dynamics in terms of spatially and temporally overlapping networks. Nature Communications 6,
684 7751. doi:10.1038/ncomms8751.
- 685 Karahanoglu, F.I., Ville, D.V.D., 2017. Dynamics of large-scale fMRI networks: Deconstruct brain
686 activity to build better models of brain function. Current Opinion in Biomedical Engineering 3,
687 28–36. doi:10.1016/j.cobme.2017.09.008.
- 688 Keilholz, S., Caballero-Gaudes, C., Bandettini, P., Deco, G., Calhoun, V., 2017. Time-resolved
689 resting-state functional magnetic resonance imaging analysis: Current status, challenges, and
690 new directions. Brain Connectivity 7, 465–481. doi:10.1089/brain.2017.0543.
- 691 Khalidov, I., Fadili, J., Lazeyras, F., Ville, D.V.D., Unser, M., 2011. Activelets: Wavelets for
692 sparse representation of hemodynamic responses. Signal Processing 91, 2810–2821. doi:10.1016/
693 j.sigpro.2011.03.008.
- 694 Kinany, N., Pirondini, E., Micera, S., Ville, D.V.D., 2020. Dynamic functional connectivity of
695 resting-state spinal cord fMRI reveals fine-grained intrinsic architecture. Neuron 108, 424–435.e4.
696 doi:10.1016/j.neuron.2020.07.024.

- 697 Lindquist, M.A., Waugh, C., Wager, T.D., 2007. Modeling state-related fMRI activity using change-
698 point theory. *NeuroImage* 35, 1125–1141. doi:10.1016/j.neuroimage.2007.01.004.
- 699 Liu, X., Chang, C., Duyn, J.H., 2013. Decomposition of spontaneous brain activity into distinct
700 fMRI co-activation patterns. *Frontiers in Systems Neuroscience* 7, 101. doi:10.3389/fnsys.
701 2013.00101.
- 702 Liu, X., Duyn, J.H., 2013. Time-varying functional network information extracted from brief
703 instances of spontaneous brain activity. *Proceedings of the National Academy of Sciences* 110,
704 4392–4397. doi:10.1073/pnas.1216856110.
- 705 Liu, X., Zhang, N., Chang, C., Duyn, J.H., 2018. Co-activation patterns in resting-state fMRI
706 signals. *NeuroImage* 180, 485–494. doi:10.1016/j.neuroimage.2018.01.041.
- 707 Lopes, R., Lina, J., Fahoum, F., Gotman, J., 2012. Detection of epileptic activity in fMRI without
708 recording the EEG. *NeuroImage* 60, 1867–1879. doi:10.1016/j.neuroimage.2011.12.083.
- 709 Loula, J., Varoquaux, G., Thirion, B., 2018. Decoding fMRI activity in the time domain improves
710 classification performance. *NeuroImage* 180, 203–210. doi:10.1016/j.neuroimage.2017.08.018.
- 711 Lurie, D.J., Kessler, D., Bassett, D.S., Betzel, R.F., Breakspear, M., Kheilholz, S., Kucyi, A.,
712 Liégeois, R., Lindquist, M.A., McIntosh, A.R., Poldrack, R.A., Shine, J.M., Thompson, W.H.,
713 Bielczyk, N.Z., Douw, L., Kraft, D., Miller, R.L., Muthuraman, M., Pasquini, L., Razi, A.,
714 Vidaurre, D., Xie, H., Calhoun, V.D., 2020. Questions and controversies in the study of time-
715 varying functional connectivity in resting fMRI. *Network Neuroscience* 4, 30–69. doi:10.1162/
716 netn_a_00116.
- 717 Madi, M.K., Karameh, F.N., 2017. Hybrid cubature kalman filtering for identifying nonlinear
718 models from sampled recording: Estimation of neuronal dynamics. *PLOS ONE* 12, e0181513.
719 doi:10.1371/journal.pone.0181513.
- 720 Meinshausen, N., Bühlmann, P., 2010. Stability selection. *Journal of the Royal Statistical Society:
721 Series B (Statistical Methodology)* 72, 417–473. doi:10.1111/j.1467-9868.2010.00740.x.
- 722 Moeller, S., Yacoub, E., Olman, C.A., Auerbach, E., Strupp, J., Harel, N., Uğurbil, K., 2010. Multiband
723 multislice GE-EPI at 7 tesla, with 16-fold acceleration using partial parallel imaging
724 with application to high spatial and temporal whole-brain fMRI. *Magnetic Resonance in Medicine*
725 63, 1144–1153. doi:10.1002/mrm.22361.
- 726 Monga, V., Li, Y., Eldar, Y.C., 2021. Algorithm unrolling: Interpretable, efficient deep learning
727 for signal and image processing. *IEEE Signal Processing Magazine* 38, 18–44. doi:10.1109/MSP.
728 2020.3016905.
- 729 Ongie, G., Jalal, A., Metzler, C.A., Baraniuk, R.G., Dimakis, A.G., Willett, R., 2020. Deep learning
730 techniques for inverse problems in imaging. *IEEE Journal on Selected Areas in Information
731 Theory* 1, 39–56. doi:10.1109/JSAIT.2020.2991563.
- 732 van Oort, E.S.B., Mennes, M., Navarro Schröder, T., Kumar, V.J., Zaragoza Jimenez, N.I., Grodd,
733 W., Doeller, C.F., Beckmann, C.F., 2018. Functional parcellation using time courses of instant-
734 taneous connectivity. *NeuroImage* 170, 31–40. doi:10.1016/j.neuroimage.2017.07.027.

- 735 Ortelli, F., van de Geer, S., 2019. Synthesis and analysis in total variation regularization.
736 arXiv:1901.06418.
- 737 Patriat, R., Molloy, E.K., Birn, R.M., 2015. Using edge voxel information to improve motion
738 regression for rs-fMRI connectivity studies. *Brain Connectivity* 5, 582–595. doi:10.1089/brain.
739 2014.0321.
- 740 Petridou, N., Gaudes, C.C., Dryden, I.L., Francis, S.T., Gowland, P.A., 2012. Periods of rest in
741 fMRI contain individual spontaneous events which are related to slowly fluctuating spontaneous
742 activity. *Human Brain Mapping* 34, 1319–1329. doi:10.1002/hbm.21513.
- 743 Pidnebesna, A., Fajnerová, I., Horáček, J., Hlinka, J., 2019. Estimating sparse neuronal signal from
744 hemodynamic response: the mixture components inference approach. bioRxiv doi:10.1101/2019.
745 12.19.876508.
- 746 Pirondini, E., Kinany, N., Sueur, C.L., Griffis, J.C., Shulman, G.L., Corbetta, M., Ville, D.V.D.,
747 2022. Post-stroke reorganization of transient brain activity characterizes deficits and recovery of
748 cognitive functions. *NeuroImage* 255, 119201. doi:10.1016/j.neuroimage.2022.119201.
- 749 Polimeni, J.R., Lewis, L.D., 2021. Imaging faster neural dynamics with fast fmri: A need for
750 updated models of the hemodynamic response. *Progress in neurobiology* 207, 102174. doi:10.
751 1016/j.pneurobio.2021.102174.
- 752 Posse, S., Wiese, S., Gembbris, D., Mathiak, K., Kessler, C., Grosse-Ruyken, M.L., Elghahwagi,
753 B., Richards, T., Dager, S.R., Kiselev, V.G., 1999. Enhancement of BOLD-contrast sensitivity
754 by single-shot multi-echo functional MR imaging. *Magnetic Resonance in Medicine* 42, 87–97.
755 doi:10.1002/(sici)1522-2594(199907)42:1<87::aid-mrm13>3.0.co;2-o.
- 756 Preti, M.G., Bolton, T.A., Ville, D.V.D., 2017. The dynamic functional connectome: State-of-the-
757 art and perspectives. *NeuroImage* 160, 41–54. doi:10.1016/j.neuroimage.2016.12.061.
- 758 Raguet, H., Fadili, J., Peyré, G., 2013. A generalized forward-backward splitting. *SIAM Journal*
759 on Imaging Sciences 6, 1199–1226. doi:10.1137/120872802.
- 760 Riera, J.J., Watanabe, J., Kazuki, I., Naoki, M., Aubert, E., Ozaki, T., Kawashima, R., 2004. A
761 state-space model of the hemodynamic approach: nonlinear filtering of BOLD signals. *NeuroIm-*
762 age 21, 547–567. doi:10.1016/j.neuroimage.2003.09.052.
- 763 Rolls, E.T., Cheng, W., Feng, J., 2021. Brain dynamics: Synchronous peaks, functional connectivity,
764 and its temporal variability. *Human brain mapping* 42, 2790–2801. doi:10.1002/hbm.25404.
- 765 Ruiz-Euler, H.C., Marques, J.R.F., Kappen, H.J., 2018. Nonlinear deconvolution by sampling
766 biophysically plausible hemodynamic models. arXiv:1803.08797.
- 767 Sadaghiani, S., Uğurbil, K., Uludağ, K., 2009. Neural activity-induced modulation of bold poststim-
768 ulus undershoot independent of the positive signal. *Magnetic resonance imaging* 27, 1030–1038.
769 doi:10.1016/j.mri.2009.04.003.
- 770 Schwarz, G., 1978. Estimating the dimension of a model. *The Annals of Statistics* 6, 461–464.
771 doi:10.1214/aos/1176344136.

- 772 Setsompop, K., Gagoski, B.A., Polimeni, J.R., Witzel, T., Wedeen, V.J., Wald, L.L., 2011. Blipped-
773 controlled aliasing in parallel imaging for simultaneous multislice echo planar imaging with re-
774 duced g-factor penalty. *Magnetic Resonance in Medicine* 67, 1210–1224. doi:10.1002/mrm.23097.
- 775 Shmueli, K., van Gelderen, P., de Zwart, J.A., Horovitz, S.G., Fukunaga, M., Jansma, J.M., Duyn,
776 J.H., 2007. Low-frequency fluctuations in the cardiac rate as a source of variance in the resting-
777 state fMRI BOLD signal. *NeuroImage* 38, 306–320. doi:10.1016/j.neuroimage.2007.07.037.
- 778 Sporns, O., Faskowitz, J., Teixeira, A.S., Cutts, S.A., Betzel, R.F., 2021. Dynamic expression of
779 brain functional systems disclosed by fine-scale analysis of edge time series. *Network neuroscience*
780 (Cambridge, Mass.) 5, 405–433. doi:10.1162/netn_a_00182.
- 781 Sreenivasan, K.R., Havlicek, M., Deshpande, G., 2015. Nonparametric hemodynamic deconvolution of
782 fMRI using homomorphic filtering. *IEEE Transactions on Medical Imaging* 34, 1155–1163.
783 doi:10.1109/tmi.2014.2379914.
- 784 Tagliazucchi, E., Balenzuela, P., Fraiman, D., Chialvo, D.R., 2012. Criticality in large-scale brain
785 fmri dynamics unveiled by a novel point process analysis. *Frontiers in physiology* 3, 15. doi:10.
786 3389/fphys.2012.00015.
- 787 Tagliazucchi, E., Balenzuela, P., Fraiman, D., Montoya, P., Chialvo, D.R., 2011. Spontaneous bold
788 event triggered averages for estimating functional connectivity at resting state. *Neuroscience
789 letters* 488, 158–163. doi:10.1016/j.neulet.2010.11.020.
- 790 Tagliazucchi, E., Siniatchkin, M., Laufs, H., Chialvo, D.R., 2016. The voxel-wise functional con-
791 nectome can be efficiently derived from co-activations in a sparse spatio-temporal point-process.
792 *Frontiers in neuroscience* 10, 381. doi:10.3389/fnins.2016.00381.
- 793 Tan, F.M., Caballero-Gaudes, C., Mullinger, K.J., Cho, S.Y., Zhang, Y., Dryden, I.L., Francis,
794 S.T., Gowland, P.A., 2017. Decoding fMRI events in sensorimotor motor network using sparse
795 paradigm free mapping and activation likelihood estimates. *Human Brain Mapping* 38, 5778–
796 5794. doi:10.1002/hbm.23767.
- 797 Tarun, A., Wainstein-Andriano, D., Sterpenich, V., Bayer, L., Perogamvros, L., Solms, M., Ax-
798 macher, N., Schwartz, S., Ville, D.V.D., 2020. NREM sleep stages specifically alter dynamical
799 integration of large-scale brain networks. *iScience* 24, 101923. doi:10.1101/2020.07.08.193508.
- 800 Tarun, A., Wainstein-Andriano, D., Sterpenich, V., Bayer, L., Perogramvos, L., Solms, M., Ax-
801 macher, N., Schwartz, S., Van De Ville, D., 2021. NREM sleep stages specifically alter dynamical
802 integration of large-scale brain networks. *iScience* 24, 101923. doi:10.1016/j.isci.2020.101923.
- 803 Tibshirani, R., 1996. Regression shrinkage and selection via the lasso. *Journal of the Royal Statistical
804 Society: Series B (Methodological)* 58, 267–288. doi:10.1111/j.2517-6161.1996.tb02080.x.
- 805 Triantafyllou, C., Hoge, R., Krueger, G., Wiggins, C., Potthast, A., Wiggins, G., Wald, L., 2005.
806 Comparison of physiological noise at 1.5 t, 3 t and 7 t and optimization of fMRI acquisition
807 parameters. *NeuroImage* 26, 243–250. doi:10.1016/j.neuroimage.2005.01.007.
- 808 Uruñuela, E., Jones, S., Crawford, A., Shin, W., Oh, S., Lowe, M., Caballero-Gaudes, C., 2020.
809 Stability-based sparse paradigm free mapping algorithm for deconvolution of functional MRI
810 data. *Proceedings of the Annual International Conference of the IEEE Engineering in Medicine
and Biology Society*, EMBS 2020-July, 1092–1095. doi:10.1109/embc44109.2020.9176137.

- 812 Uruñuela, E., Moia, S., Caballero-Gaudes, C., 2021. A low rank and sparse paradigm free mapping
813 algorithm for deconvolution of fMRI data doi:10.1109/isbi48211.2021.9433821.
- 814 Uruñuela-Tremiño, E., Moia, S., Gonzalez-Castillo, J., Caballero-Gaudes, C., 2019. Deconvolution
815 of multi-echo functional MRI data with multivariate multi-echo sparse paradigm free mapping.
816 ISMRM 27th Annual Meeting and Exhibition .
- 817 Yeşilyurt, B., Uğurbil, K., Uludağ, K., 2008. Dynamics and nonlinearities of the bold response at
818 very short stimulus durations. Magnetic resonance imaging 26, 853–862. doi:10.1016/j.mri.
819 2008.01.008.
- 820 Zhang, X., Pan, W.J., Keilholz, S.D., 2020. The relationship between BOLD and neural activity
821 arises from temporally sparse events. NeuroImage 207, 116390. doi:10.1016/j.neuroimage.
822 2019.116390.
- 823 Zoeller, D., Sandini, C., Karahanoglu, F.I., Schaer, M., Eliez, S., Van De Ville, D., 2019. Large-
824 scale brain network dynamics provide a measure of psychosis and anxiety in 22q11.2 deletion
825 syndrome. Biological Psychiatry: Cognitive Neuroscience and Neuroimaging 4, 881–892. doi:10.
826 1016/j.bpsc.2019.04.004.
- 827 Zöller, D., Sandini, C., Karahanoglu, F.I., Padula, M.C., Schaer, M., Eliez, S., Ville, D.V.D.,
828 2019. Large-scale brain network dynamics provide a measure of psychosis and anxiety in 22q11.2
829 deletion syndrome. Biological Psychiatry: Cognitive Neuroscience and Neuroimaging 4, 881–892.
830 doi:10.1101/551796.

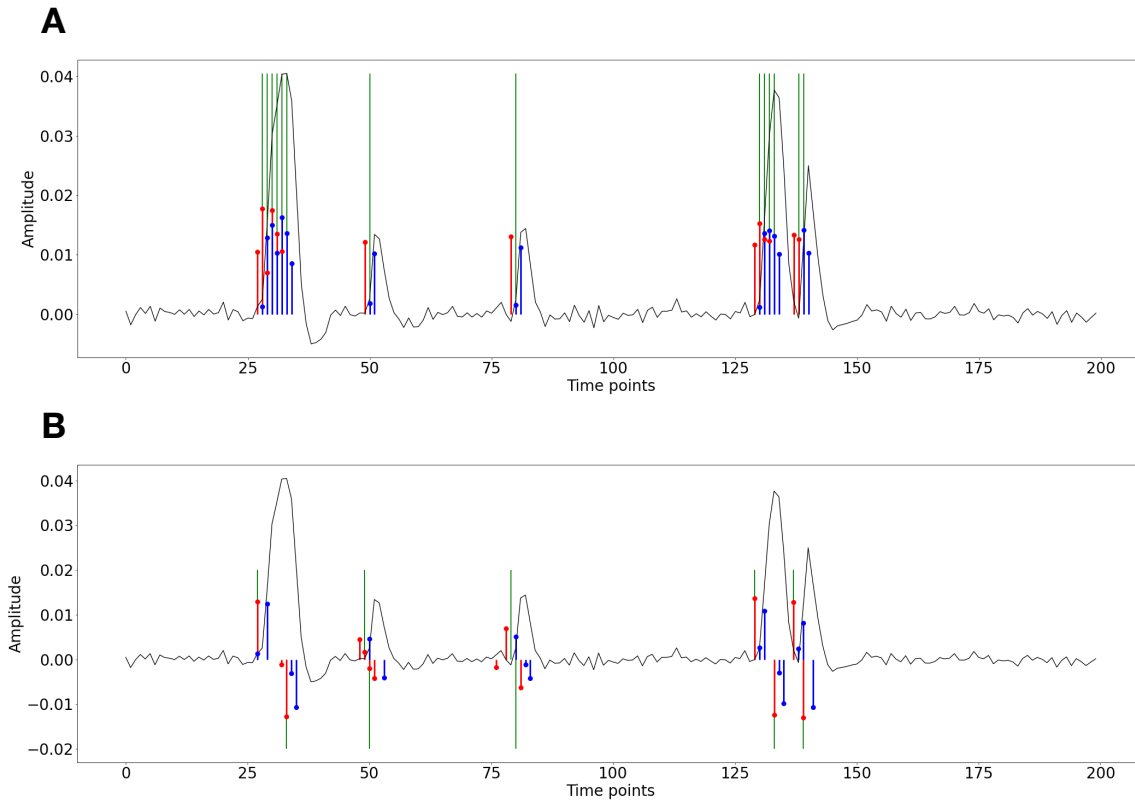


Figure S1: Activity-inducing (A) and innovation (B) signals estimated with PFM (red) and TA (blue) using their built-in HRF as opposed to using the same. The black line depicts the simulated signal, while the green lines indicate the onsets of the simulated neuronal events. X axis shows time in TRs.

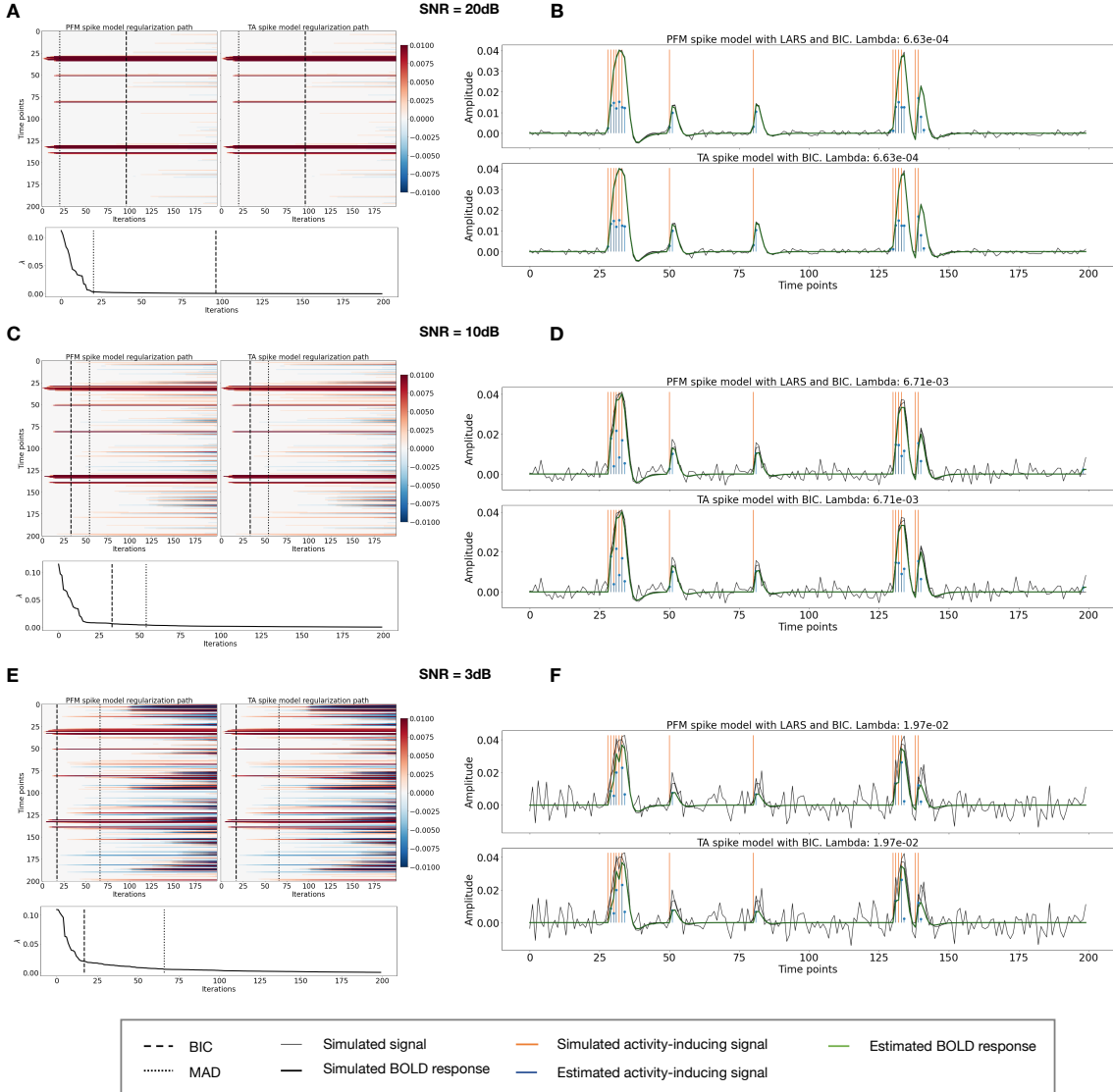


Figure S2: Spike model simulations. (Left) Heatmap of the regularization paths of the activity-inducing signal estimated with PFM and TA as a function of λ (increasing number of iterations in x-axis), whereas each row in the y-axis shows one time-point. Vertical lines denote iterations corresponding to the Akaike and Bayesian Information Criteria (AIC and BIC) optima. (Right) Estimated activity-inducing (blue) and activity-related (green) signals when set based on BIC. All estimates of are identical, regardless of SNR.

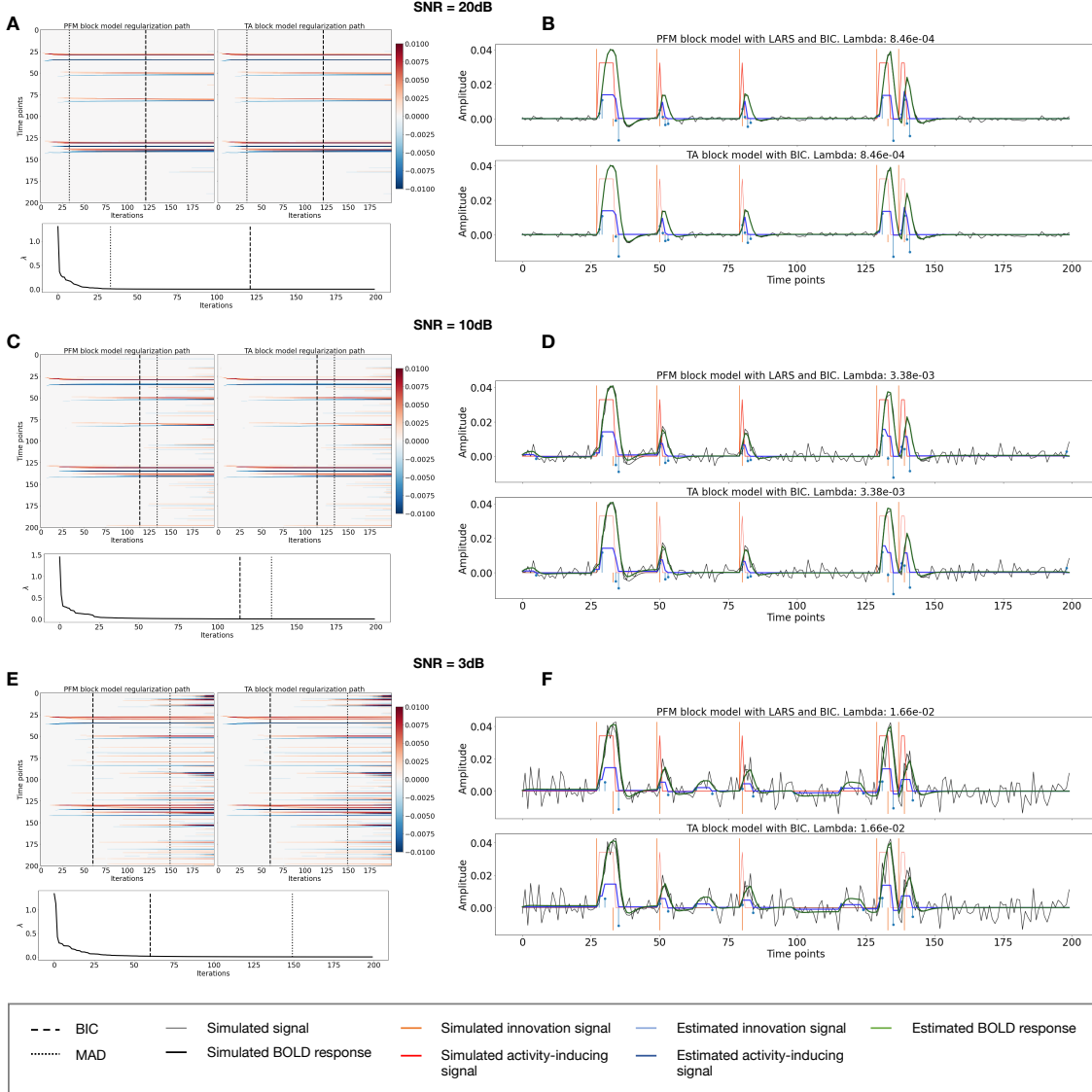


Figure S3: Block model simulations. (Left) Heatmap of the regularization paths of the innovation signal estimated with PFM and TA as a function of λ (increasing number of iterations in x-axis), whereas each row in the y-axis illustrates one time-point. Vertical lines denote iterations corresponding to the Akaike and Bayesian Information Criteria (AIC and BIC) optima. (Right) Estimated innovation (blue) and activity-related (green) signals when λ is set based on BIC. All the estimates are identical when compared between the PFM and TA cases, regardless of SNR.

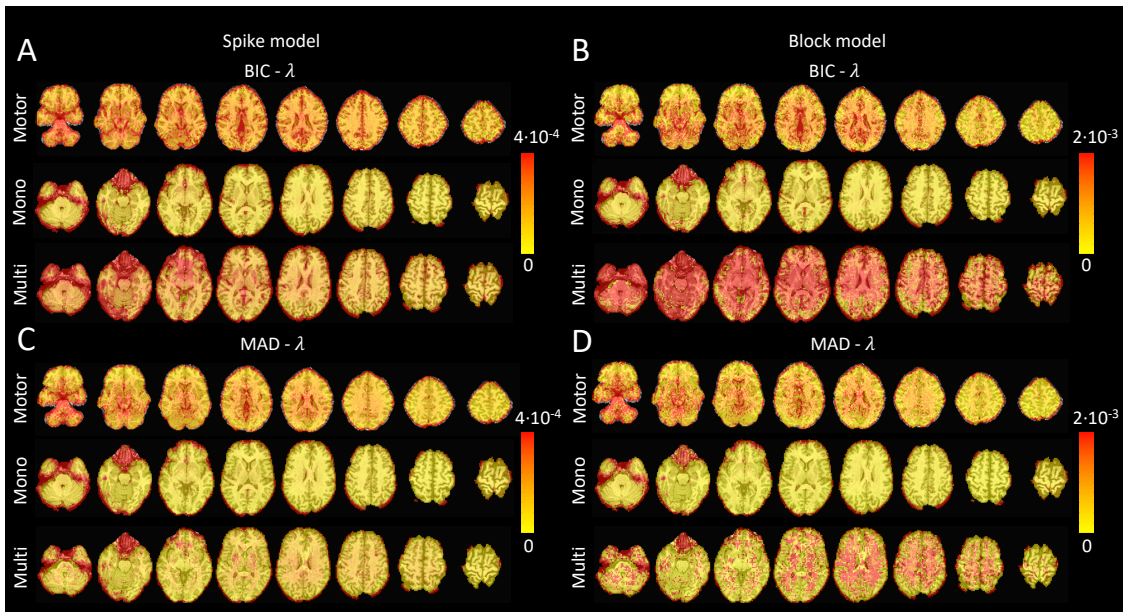


Figure S4: Values of λ across the different voxels in the brain used to estimate (A) the activity-inducing signal (spike model) and (B) the innovation signal (block model) with the BIC selection, as well as (C) the activity-inducing signal (block model) and (D) the innovation signal (block model) with a MAD-based selection. The λ maps are shown for the three experimental fMRI datasets: the motor task (Motor), the monoband resting-state (Mono), and the multiband resting-state (Multi) datasets.

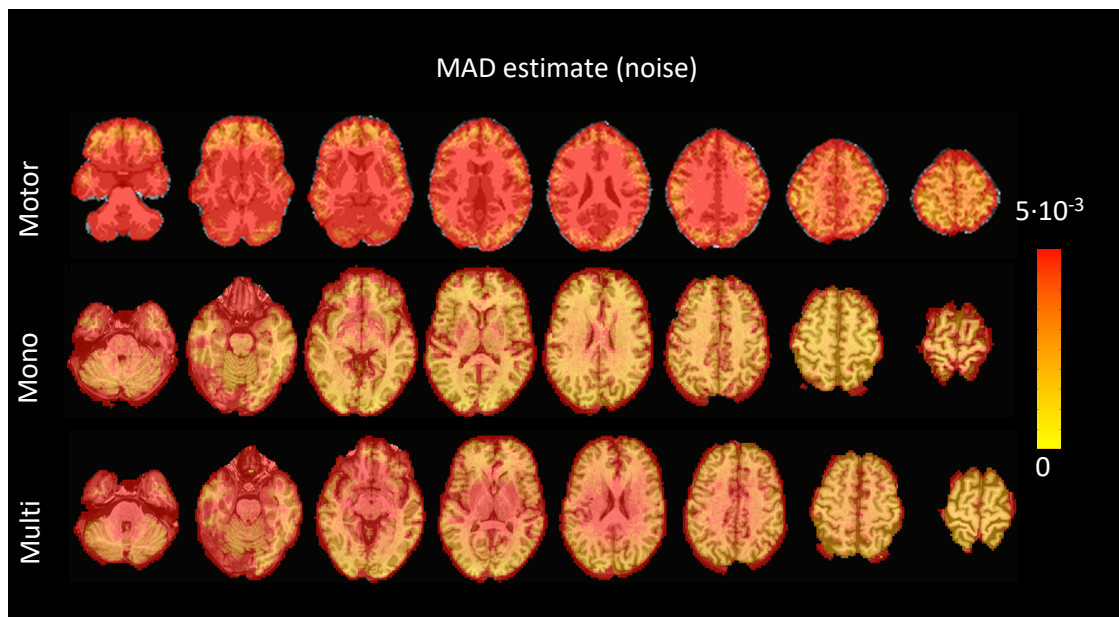


Figure S5: Values of the MAD estimate of standard deviation of the noise across the different voxels in the brain for the three experimental fMRI datasets: the motor task (Motor), the monoband resting-state (Mono), and the multiband resting-state (Multi) datasets.

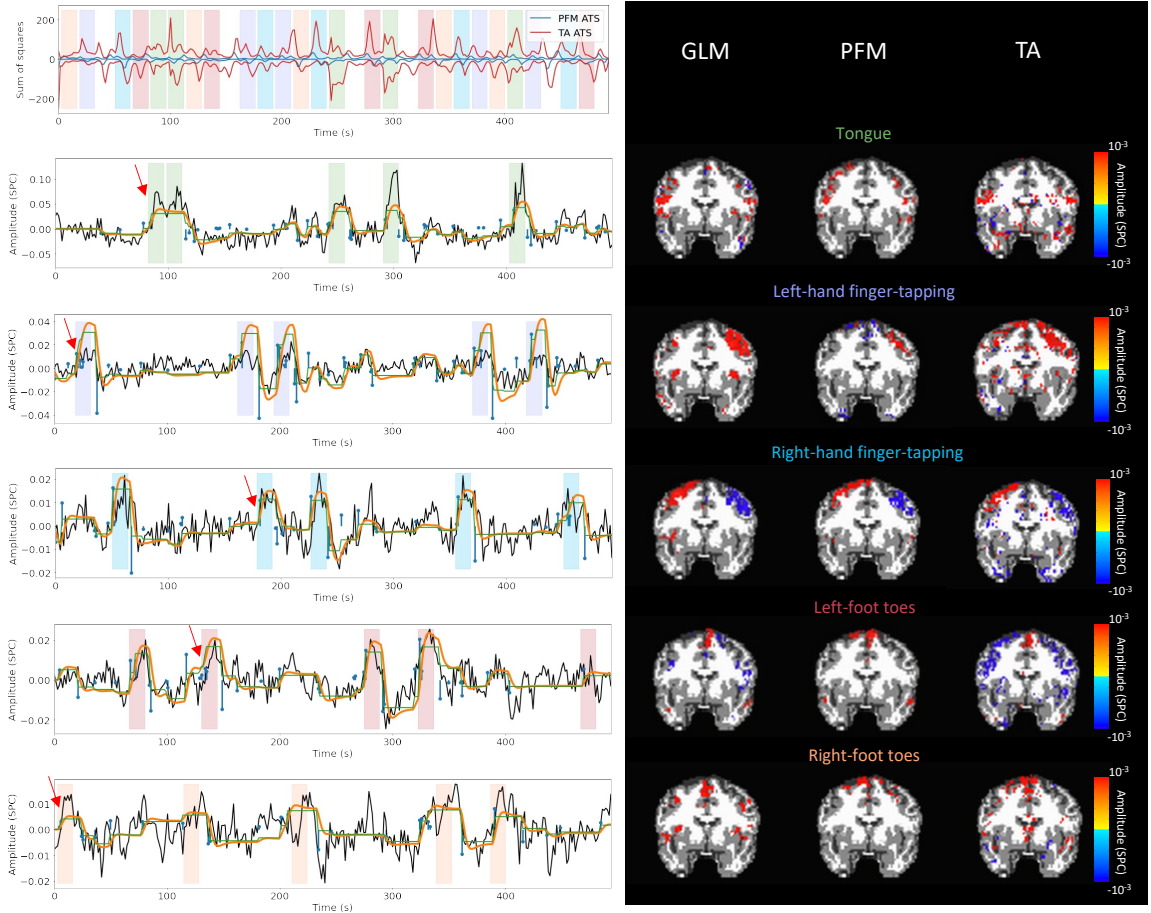


Figure S6: Activity maps of the motor task using a selection of λ based on the MAD estimate. Row 1: Activation time-series of the innovation signals estimated by PFM (in blue) or TA (in red) calculated as the sum of squares of all voxels at every timepoint. Positive-valued and negative-valued contributions were separated into two distinct timecourses. Color-bands indicate the onset and duration of each condition in the task (green: tongue, purple: left-hand finger-tapping, blue: right-hand finger-tapping, red: left-foot toes, orange: right-foot toes). Rows 2-6: time-series of a representative voxel for each task with the PFM-estimated innovation (blue), PFM-estimated activity-inducing (green), and activity-related (i.e., fitted, orange) signals, with their corresponding GLM, PFM, and TA maps on the right. The maps shown on the right are sampled at the time-point labeled with the red arrows and display the innovation signals at that moment across the whole brain.

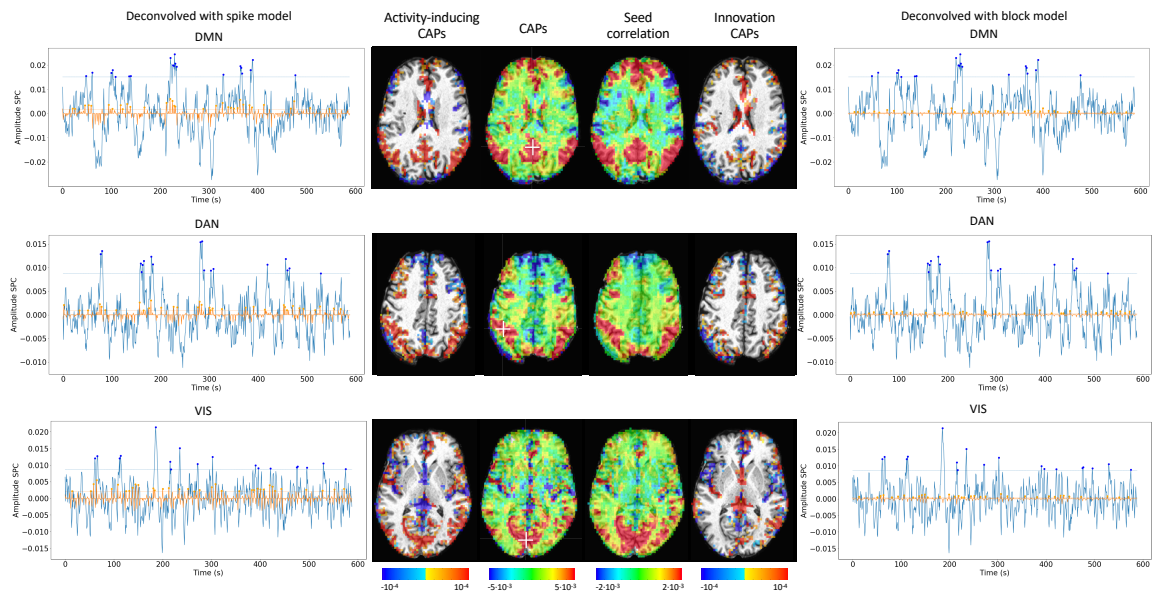


Figure S7: Activity-inducing CAPs (left) and innovation CAPs (right) obtained with the PFM-estimated activity-inducing and innovation signals respectively, using a MAD-based selection of λ . Time-points selected with a 95th percentile threshold are shown over the average time-series (blue) in the seed region (white-cross) and the deconvolved signal (orange). CAPs and seed correlation maps are illustrated in the center.